MEASURING ACTINIDE PARTITIONING IN ZIRCON TO IMPROVE THE ^{230}Th CORRECTION FOR ^{206}Pb/^{238}U DATES

BY

ASHLEY COCCIADIFERRO

Submitted to the graduate degree program in Geology and the Graduate Faculty of the University of Kansas in partial fulfillment of the requirements for the degree of Master of Science.

_____

Chairperson Noah M. McLean

_____

Andreas Möller

_____

Jennifer Roberts

Date Defended: December 19, 2019

The Thesis Committee for ASHLEY COCCIADIFERRO certifies that this is the approved version of the following thesis:

MEASURING ACTINIDE PARTITIONING IN ZIRCON TO IMPROVE THE ^{230}Th CORRECTION FOR ^{206}Pb/^{238}U DATES

_____

Chairperson Noah M. McLean

Date approved: December 19, 2019

ABSTRACT

The element Th, and its isotope ^{230}Th, an intermediate daughter isotope in the ^{238}U decay series, is often excluded relative to U from the mineral zircon during crystallization. Zircon is geochronologically important because it incorporates U, but when Th is excluded, a deviation from secular equilibrium occurs. The return to secular equilibrium, where the parent nuclide and intermediate daughter products have equal activities, results in a deficit of stable daughter ^{206}Pb. This causes measured zircon $^{206}Pb/^{238}U$ dates to be up to ~109 ka too young, necessitating a correction for the initial ^{230}Th deficit by comparing the Th/U_{zircon} to an estimated Th/U_{melt} and calculating a fractionation factor. For many Cenozoic zircon analyses, uncertainty in this factor makes up a majority of the uncertainty budget because existing Th-U partitioning studies of synthetic and natural samples are imprecise (e.g. Burnham and Berry, 2012; Luo and Ayers, 2009; Rubatto and Hermann, 2007).

We have synthesized zircon from a range of temperatures (1200 to 1350ºC), melt compositions (basaltic andesite to andesite), and oxygen fugacities (QFM-4 to QFM+4), all doped with 500-1000 ppm U and Th. By analyzing whole crystals using isotopic dilution methods and high-spatial resolution SIMS analyses, we have reduced the uncertainty on D_{Th}/D_U to 1-5 %.

With higher resolution, we found that D_{Th}/D_U generally decreases with f_{O2} and increases with temperature and melt composition. The variation in our datasets we attribute to the sector zoning that can be seen in cathodoluminescence (CL) images of our samples. Dark sectors generally had higher D_{Th}/D_U ratios than light sectors. We were able to sample light and dark sectors with EMPA and SIMS spots and observed that weighted mean D_{Th}/D_U of our ID-ICPMS analyses existed inside the range of the ratios found in light and dark sectors.

Using these measurements, we demonstrate that trace element partitioning varies on a micron-scale in zircon, but that whole-crystal D_{Th}/D_U can be applied to natural samples by estimating the volume ratio of light dark sectors.

These D_{Th}/D_U ratios can be used to calculate ^{230}Th corrections for zircon grown under similar oxygen fugacities, melt compositions, and temperatures to improve analytical uncertainties on $^{206}Pb/^{238}U$ dates. These higher precision dates can then be used to resolve rapid geologic processes like incremental pluton assembly (e.g., Mills and Coleman, 2013) or better constrain timescales of mass extinction and biotic recovery (e.g., Schoene et al., 2015).

ACKNOWLEDGEMENTS

This work was initiated and supported by Dr. Noah McLean and Dr. Michael Krawcyznski. The mentorship of Dr. Noah McLean was invaluable throughout the past two and a half years. Dr. Joe Andrew and Dr. Andreas Moller devoted much time and energy to improving this work. Thanks are owed to Julie Sophis and Christine Chan for their friendship and camaraderie during late nights in the lab. Insightful comments from Julie Sophis, Clark Sturdevant, Christine Chan, Dr. Andreas Moller, and Dr. Noah McLean are greatly appreciated. Special thanks to Julie Sophis, Christine Chan, Jack Touran, and Dr. Michael Krawcyznski for sharing unpublished data. Thanks are owed to all KU geology graduate students for their friendship. Support for this project comes from the National Science Foundation and the Geological Society of America.

TABLE OF CONTENTS

INTRODUCTION

U-Pb zircon geochronology is an important chronometer, used across the Earth Sciences. Part of its power is a dual decay system, where ^{238}U and ^{235}U, with half lives of 4.5 Gyr and 704 Myr (Jaffey et al., 1971), decay to ultimate daughters ^{206}Pb and ^{207}Pb. For the Cenozoic, the $^{206}Pb/^{238}U$ chronometer is used almost exclusively because of the greater abundance of these isotopes. The U-bearing accessory mineral zircon is common in felsic and less commonly found in mafic igneous systems. Zircon has reliable U-Pb dates because, first, U is preferentially partitioned into the crystal while Pb is effectively excluded (e.g., Watson et al., 1997), which eliminates the need to correct for initial Pb. Second, it has a high closure temperature for Pb diffusion, meaning U-Pb dates are not reset by subsequent heating events (Cherniak and Watson, 2001, Heaman and Parrish, 1991). Finally, zircon is resistant to chemical or physical weathering, even appearing as Hadean detrital grains in the Jack Hills metaconglomerate (e.g., Wilde et al., 2001; Wyche et al., 2004).

Dating zircons using the U-Pb system can solve a wide variety of geologic questions, like dating volcanic eruptions (e.g., the Bishop Tuff; Crowley et al., 2007), determining maximum depositional ages (e.g., in basins within the Andes; DeCelles et al., 2007), putting age constraints on mass extinctions (e.g., the end-Cretaceous; Schoene et al., 2019) or determining timescales of crustal formation (e.g., at mid-ocean ridge spreading centers; Lissenburg et al., 2009). U-Pb zircon geochronology has significantly improved in accuracy with the advent of the CA-ID-TIMS technique (Mattinson, 2005; Widmann et al., 2019) and precision with decreasing laboratory Pb blanks. At present, $^{206}Pb/^{238}U$ ratios in zircon can be measured with better than 0.05% precision (Schoene, 2014) for zircons that are at least ~10 million years old. Improved precision on crystals younger than 10 Ma could resolve geologic processes that occur at faster

rates or over short timescales, like the evolution of a volcanic system (e.g. Tappa et al., 2011). Understanding the processes that precede and trigger large volcanic eruptions could help researchers predict catastrophic events. But for < 10 Ma zircons, and most Cenozoic-aged zircons, a correction for initial ^{230}Th disequilibrium within the ^{238}U decay chain (Fig. 1) is now often the limiting source of analytical uncertainty. This prevents workers from dating younger crystals to the same precision as grains older than the Cenozoic.

Initial ^{230}Th disequilibrium occurs during zircon crystallization, when U is usually preferentially partitioned into the zircon crystal lattice over Th (Mattinson, 1973). The result is a deficiency of ^{230}Th in the ^{238}U decay series and a deviation from secular equilibrium. Secular equilibrium requires that each parent decay rate is the same as its intermediate daughter's, so that the activities of the parent and daughter isotopes are equal. Since ^{230}Th is an intermediate daughter product of the ^{238}U decay series (Fig. 1) and has a relatively long half-life (~76 ka; Cheng et al., 2013), it is abundant enough to produce a measurable deficit of ^{206}Pb (e.g., Schärer, 1984). Accurately dating a zircon using the ^{206}Pb/^{238}U date requires a correction for this deficit of ^{206}Pb, but other isotopic dating systems, such as ^{238}U-^{230}Th U-series zircon dating, exploit this deviation from secular equilibrium. Other isotopes in the decay series either have half-lives that are too short to result in a significant excess or deficit in ^{206}Pb, or, as in the case of ^{234}U, are not isotopically fractionated by the crystal (e.g., Schärer, 1984).

By contrast to the U-Pb system, ^{238}U-^{230}Th U-series zircon dating quantifies the return to secular equilibrium and can be used to examine the rates and timescales of fractionation processes (Bourdon et al., 2003; Ried et al., 1997). The U-series system can be used for zircon crystals that are up to five times older than the half-life of ^{230}Th, about 400 ka. Samples with a

range of $^{238}U/^{232}Th$ ratios are required to create an isochron to determine the age of the system or fractionation event (e.g., zircon crystallization ages in rhyolite, Stelten and Cooper, 2012).

Since the U-series system can only date zircons up to 400 ka, $^{206}Pb/^{238}U$ dates, are more widely used to date zircons across the rest of geologic time. For Cenozoic zircon older than 400 ka, we must correct for ^{230}Th intermediate daughter disequilibrium. This correction can make up a large portion of the uncertainty budget, which prevents researchers from dating Cenozoic zircons to the same 0.05% precision as older grains (Ickert et al., 2015).

There are two ways to formulate the equation for a ^{230}Th correction for zircon dated using a $^{206}Pb/^{238}U$ ratio (McLean et al., 2011). The first method, shown in equation (1), measures $(Th/U)_{zircon}$, estimates $(Th/U)_{melt}$ using melt inclusions if available, geochemical models based on whole rock analyses, or geochemical compilations, and calculates a fractionation factor. The second method, represented by equation 2, uses empirical measurements to estimate zircon relative Th/U partitioning in the term D_{Th}/D_U.

$$(1) \qquad \frac{^{206}Pb}{^{238}U} = e^{\lambda_{238}t} - 1 + \frac{\lambda_{238}}{\lambda_{230}}\left[\left(\frac{Th}{U}\right)_{zircon} / \left(\frac{Th}{U}\right)_{melt} - 1\right]$$

$$(2) \qquad \frac{^{206}Pb}{^{238}U} = e^{\lambda_{238}t} - 1 + \frac{\lambda_{238}}{\lambda_{230}}\left[\left(\frac{D_{Th}}{D_U}\right) - 1\right]$$

In these two equations, λ_{238} and λ_{230} are the ^{238}U and ^{230}Th decay constants, t is the age of the crystal, and D_{Th} and D_U are the Th and U zircon-melt partition coefficients.

The partition coefficients D_U and D_{Th} describe the behavior of Th and U during zircon crystallization. A partition coefficient (D) is the ratio of the concentrations of an element in the crystal and the melt at equilibrium:

$$(3) \qquad D_U = [U]_{zircon}/[U]_{melt}$$

For the past two decades, the ^{230}Th correction has most frequently been made using equation (1). This is because it is more precise to estimate U/Th partitioning using the measured zircon Th/U and an estimate of the magma Th/U from which it crystallized than to use the large experimental uncertainties (> 50%) on D_U and D_{Th}.

Previous workers (Luo and Ayers, 2009; Rubatto and Hermann, 2007; Burnham and Berry, 2012) have successfully determined partition coefficients of large suites of trace elements in zircon, but their D_{Th} and D_U values have uncertainties too large for our purposes. Three studies focused on describing trace and major element partitioning in zircon under a set of experimental parameters, including temperature, pressure, and oxygen fugacity.

Rubatto and Hermann (2007) observed that partition coefficients varied as a function of temperature from 800 to 1050 C and 2 GPa for experimentally grown garnet and in a ~ 80% granite mix and ~ 20% hydrous garnet mix. D_{Th}/D_U increased with increasing temperature over this temperature range (Fig. 5). They determined partition coefficients for zircon and garnet within that temperature range at 2 GPa for P, Y, REE, Zr, Hf, Th, and U. Experimentally grown zircons were small, generally less than 5 μm in diameter at 800 and 850 C.

D_{Th}/D_U from Luo and Ayers (2009) also shows a slight increase within uncertainty from 900 to 1300 C at 1.5 GPa. Zircons were on average 5-20 μm in diameter. However, measurements of their experiments at 800 C and 0.1 - 0.2 GPa show a much wider range of D_{Th}/D_U than Rubatto and Hermann (2007). They focused on the temperature and pressure effects of elemental partitioning in zircon grown in peralkaline rhyolites, measuring partition coefficients for P, Sc, Ti, V, Y, La, Ce, Pr, Nd, Eu, Gd, Ho, Yb, Lu, Hf, Th, and U. D_{Th} and D_U generally decrease with temperature and pressure within 1 σ analytical uncertainty. There does not appear to be a relationship between pressure and D_{Th} or D_U for experiments run at 800 C.

Since temperature and pressure are increased for other experiments, we cannot resolve the parameter that controls the observed decrease in D_{Th} and D_U. However, since Rubatto and Hermann (2007) observed decreases in D_{Th} and D_U with increasing temperature, it is more likely the parameter that affects these partition coefficients.

Burnham and Berry (2012) performed experiments on andesitic compositions at temperatures of 1300 C, measuring the dependence of partitioning behavior of a variety of trace elements, including U and Th, on oxygen fugacity. Over a wide range of oxygen fugacities ($\log_{fO2}$ = -14 - 0, ΔQFM = -7.7 - 6.3), the authors found that D_{Th} is invariant, but that D_U decreases by an order of magnitude.. Burnham and Berry (2012) propose that D_U decreases at high f_{O2} because U oxidizes to U^{6+} and no longer fits well into the zircon crystal structure. They also determined partition coefficients of a number of trace and some major elements- REEs, Ta, Ti, Hf, Mg, Si, Ba, Nb, Sc, Sr, Y, Ca over this range of experimental conditions.

Because experiments from these three publications focused on a long list of major and trace elements, they generally had low analytical precision (> 50%) for D_U and D_{Th} measurements. This reflects both low levels of doping for U and Th as well as analytical protocols that are not optimized to measure them. Therefore, using these measurements in equation (2) to calculate a ^{230}Th correction is less precise than measuring the Th/U of the zircon and reasonably estimating the Th/U of the melt from which it crystallized (equation 1). By focusing on doping with high amounts (~500 - 1000 ppm) of U and Th and analyzing only U and Th, this study attempts to better understand U and Th partitioning behavior in zircon, paving the way for using equation (2) and precluding the need to tie the accuracy of $^{206}Pb/^{238}U$ dates on an estimate of melt Th/U ratios.

METHODS

Experimental synthesis:

All experiments were synthesized at the ESPM laboratory at Washington University in Saint Louis in 1 atm gas mixing vertical tube furnaces under varying f_{O2} and temperature. Table 1 shows the compositions of the starting materials used in experiments. Table 2 shows the temperatures, f_{O2}, and starting compositions of each experiment. The starting material powders were packed into a 60 mg pellet and fused onto an Fe-electroplated Pt wire loop using an oxygen-acetylene torch. The Pt loops were electroplated with Fe to minimize the gain or loss of Fe during the run. The sample was suspended on another thin Pt quench wire inside the furnace. This quench wire was hung from an alumina sample holder rod. This apparatus was placed into the furnace set at the conditions in Table 2.

The temperature of the furnace was monitored by two thermocouples with an accuracy of ± 3 C and controlled by a Eurotherm 3504 PID controller and a silicon-controlled rectifier (SCR). The f_{O2} was monitored using a yttria-doped $SIRO_2$ oxygen sensor from Ceramic Oxide Fabricators, calibrated at the Ni-NiO oxygen buffer with an accuracy of ± 2 mV or ± 0.05 log(f_{O2}) units and controlled using H_2 and CO_2 gases. Flow rates were controlled by two Alicat automatic mass flow controllers.

To start each experiment, samples were held for 10 to 24 hours over 100 C above a calculated liquidus temperature. Liquidus temperatures were estimated using the rhyolite-MELTS (Gualda et al., 2012) algorithm of the dry starting materials. Holding samples at this high of a temperature ensured any previous nucleation points were melted and homogenized within the sample. After the initial high temperature period, samples were cooled 1 - 10 C per hour until the final temperature was reached. Each experiment was kept at the final temperature

for 24 - 48 hours. Temperature conditions are listed in Table 2. To finish an experiment, the Pt quench wire was melted by running a high current through it. The sample then dropped into a 500 mL beaker of DI water and quenched to a glass. The f_{O2} conditions were maintained until approximately 2 seconds prior to quenching to minimize possible oxidation by air. Individual experiments ranged from 48 to 168 hours in total.

Secondary ion mass spectrometry (SIMS) Methods:

Grain mount procedure:

Both loose zircon grains and fragments of the experimental charge were mounted in epoxy for SIMS analyses. To analyze the single grains, samples were hand-crushed with a ceramic mortar and pestle and transferred to a small petri dish. Zircon separates were hand-picked, and larger zircons placed into a Teflon beaker. About 250 µL of cold, concentrated HF was added to the beaker for 3-5 minutes to remove residual glass.

Before removing the HF, zircons grains were visually inspected under a microscope to assure all glass had been removed. Then about 80% of the HF was removed. Samples were rinsed three times each with MilliQ water. Between each rinse, roughly 80% of the liquid was removed.

After leaching, all water was removed from the beaker and zircons were hand picked out of the beaker and placed on the top side of double-sided tape. The bottom side of the tape was placed on a thick, flat, glass slide and all air bubbles were pressed out. An outline of the 25-mm round used to pour the epoxy mount was drawn onto the back of the glass. Reference materials 91500 and SRM 610 were placed in the middle and samples were placed around the standards like the spokes of a wheel. The zircon megacryst 91500 was used as a zircon reference material because of its consistent Th/U ratio (Wiedenbeck et al., 1995, Wiedenbeck et al., 2004). SRM

610 was used as a glass standard because it contains ~500 ppm of U and Th, which is similar to sample concentrations based on preliminary data from initial sample mixes.

Mounts were ground and polished, finishing with a 0.05 µm alumina grit. Pads were rinsed with DI water every 3 to 5 minutes or if new scratches were observed. Once polishing was completed, the mount was ready to be prepped for SIMS analysis.

SIMS analyses:

A Cameca IMS-7f-GEO SIMS housed at Washington University in St. Louis, MO was used to analyze experimental zircon and glass run products with a -13 kV accelerating voltage and a 11-15 nA O^- beam focused to a spot diameter of ~20 µm. The sample was at a voltage of +8.5 kV. The mass analyzer was run at a resolution of about 2000 using entrance and exit slits. Secondary ion intensities were measured on an electron multiplier in pulse counting mode using magnetic peak hopping. The masses analyzed in the glass and zircon were $^{94}Zr^{16}O$, $^{232}Th^{16}O$, and $^{238}U^{16}O$. These masses were chosen to eliminate any mass interferences, and therefore measurements were made in the middle of peaks.

Reference zircon 91500 and SRM 610 glass were used as standards. Data reduction employed Excel macros developed at the NordSIM facility in Stockholm. Zircon data were normalized to 91500 using a Th/U = 0.3444, an average of the two isotope dilution measurements from Wiedenbeck et al. (1995). Glass measurements were normalized to SRM 610 using a Th/U = 0.9781, calculated from concentrations listed in Jochum et al. (2011).

ID-ICPMS Methods:

Gravimetric solution:

A gravimetric solution of U and Th was mixed, and the masses of each component measured to dope experiments, for use as a standard when calibrating a new ^{229}Th-^{235}U isotopic tracer, and for use as a standard for single grain ICPMS analyses.

FEP bottles (Savillex) were acid cleaned and blank checked for U prior to making the gravimetric solution. All four bottles had U blanks of 1 pg or less. The empty 1 L bottle was emptied of all cleaning acids, dried on a hot plate and its empty mass was recorded.

All masses were measured using a Mettler Toledo UMX2 and Mettler P1200. To check the linearity and determine the uncertainty of the Mettler Toledo UMX2, we weighed calibration weights on the day of mixing and several days prior. Single weights and combinations were measured across the scales mass range from 100 to 2000 µg. Atmospheric conditions (temperature, pressure, relative humidity, time) were collected for each weighing to make air buoyancy corrections.

Two certified reference materials—CRM66-7 (ThO_2) and CRM112a (U metal) were used to mix the gravimetric solution. CRM66 is a ThO_2 standard containing seven vials of ThO_2 powder. CRM66-7 is the purest of with a calculated purity of 0.9999402 wt% ThO_2. CRM112a is a normal U bar with purity of 0.999777 wt% U (New Brunswick Laboratory (NBL), 2008, Condon et al., 2010).

Weighing ThO2:

Small tin weighing boats were used to weigh the ThO_2 and U. Before adding the ThO_2, the empty boat was weighed five times. Between each measurement, the scale was tared. To create this gravimetric solution, we used a new, sealed and previously unopened bottle of CRM66-7. Each measurement was recorded 30 seconds after placing the empty boat on the scale to allow the scale to stabilize. After recording five measurements, the empty boat was

placed onto a tray to be filled with ThO_2 powder. CRM66-7 powder scooped into the tin weighing boat and immediately weighed for 30 seconds before recording the mass. Five masses were recorded, but the mass of the ThO_2 powder increased over the weighing. This was likely the result of hydration, as the room was warm and humid and ThO_2 is hygroscopic. We therefore consider the initial recorded ThO_2 mass to be the most accurate. Once the ThO_2 was poured into the 1 L FEP bottle, the empty boat was re-weighed five times to ensure no ThO_2 powder remained in the boat. To keep Th from leaching into the 1 L fluorinated ethylene propylene (FEP) bottle, dilute HF (0.005 M) was added to the concentrated HNO_3 (14.4 M) to dissolve the ThO_2 and U. Both acids were blank checked for U, which was used as a proxy for Th. The 1 L bottle was weighed with the acids and after the ThO_2 powder was added (Table 2).

Weighing U:

A ~0.6 g piece of a 4 g bar of CRM112a was cut off with a pair of hardened steel 24-inch bolt cutters. This portion was then placed in glass petri dish filled with 7 N HNO_3 for an hour to remove oxidation from the outside of the bar. After this time there was still significant oxidation, so the acid was replaced with 14.4 N HNO_3. The bar was left for 20 minutes in the 14.4 N HNO_3 and it was agitated with a pair of plastic forceps three times. While the 4 g bar of CRM112a was in the 14.4 N HNO_3, an empty tin weighing boat was weighed five times. The scale was tared between each weighing and 30 seconds was given for the scale to stabilize before recording.

After oxidation was sufficiently removed and the bar appeared to have a smooth, bright surface finish, it was placed in a glass petri dish filled with MilliQ water to rinse off the HNO_3. After the MilliQ rinse, the U piece was placed in a petri dish filled with acetone to rinse off the water and remove any liquid from the surface. The U was then transferred to the empty tin weighing boat and set on the tared scale to be continuously weighed for 5.5 minutes. Masses

were recorded at 30 second intervals. After 5.5 minutes, the scale was tared, and the U was re-weighed three times. Measurements were recorded after the scale stabilized for 30 seconds. We consider the lowest U mass measured, after evaporation of the acetone but before further surface oxidation, to be the most accurate. After weighing, the U was placed into the 1 L bottle with the ThO_2 and 14.4 N HNO_3 + 0.005 HF. The total bottle mass was recorded, and the bottle was placed on a hot plate at ~90 C until the U and ThO_2 were completely dissolved (Table 2).

Mixing the isotopic tracer:

To make precise isotope dilution measurements of U/Th ratios of zircon and glass in each sample, we mixed an isotopic tracer using ^{229}Th and ^{235}U solutions. The ^{229}Th solution was provided by John Cottle (UCSB) and the ^{235}U solution was SRM-970 dissolved in concentrated HNO_3. To quantify the elemental and isotopic purity of these solutions, 10 diluted aliquots of each were measured using an Element 2 single collector ICPMS.

After purity was quantified, the tracer isotopes were mixed. The desired concentrations of the tracer isotopes were optimized to approximate the experimental zircon U and Th concentrations. Prior to mixing, one FEP dropper bottle was precleaned with HF and HCl then blank checked. The ^{235}U and ^{229}Th solutions were decanted into this bottle and diluted to the desired concentrations of 40.9 ppb and 20.7 ppb, respectively, with blank checked 1 N HNO_3 + 0.005 N HF. The bottle was left for 2 days to equilibrate.

To calibrate the tracer, ten aliquots of the gravimetric solution were diluted and mixed with ~0.008 g spike each. These were left for over 24 hours to equilibrate then measured on the ThermoFisher Element 2 ICPMS at the University of Kansas Isotope Geochemistry Laboratory (KU IGL). The $^{235}U/^{229}Th$ ratio was estimated using a numerical inversion approach in a MATLAB script, determining the ratio using the known isotopic compositions of the gravimetric

solution, ^{229}Th solution, and ^{235}U solution. After calibration, the tracer was used to determine column and total procedural blanks prior to dissolution of samples.

Column calibration:

To minimize laboratory blank, we reduced ~ 2 mL column volumes from the anion exchange column procedure of Tissot and Dauphas (2015) to ~50 μL (Table 1). The revised procedure was tested by collecting several aliquots and measured using the ThermoFisher Element 2 ICPMS at KU IGL.

To calibrate these columns, a visually clean glass separate of H049 was hand-picked under a petrographic microscope. One ~100 μm shard was chosen, rinsed of any ethanol, and dissolved overnight on a hotplate roughly 500 μL of HF. After dissolution, the liquid was pipetted off, dried, brought up in concentrated HNO_3, dried, and brought up in the 3N HNO_3 loading solution.

UTEVA resin was hydrated in 0.05 N HCl. Before use, the resin was rinsed with 0.05 N HCl to remove any elemental contaminants from the resin. The resin was then loaded into a 50 μL column, and the procedure outlined in Table 1 was followed.

All aliquots listed in Table 1 were dried, brought up in a 1N HNO_3 + 0.005N HF solution and run on the ThermoFisher Element 2 ICPMS in wet plasma mode at KU IGL. The calibration curve in Fig. 2 was generated from the data demonstrates that separation of U and Th from each other and matrix elements matches Tissot and Dauphas (2015). After the columns were calibrated and column blanks were sufficiently clean, Th and U in experimental zircon and glass were separated using the procedure (Table 1).

Individual grain analysis preparation:

Each zircon aliquot for ID-ICPS was leached in ~ 250 µL of cold HF for 3-5 minutes, followed by three rinses with MilliQ water. Zircons were then pipetted out of the water and into microcapsules. Each microcapsule was then spiked with a weighed drop of the KU-229-235 tracer and ~75 µL of HF was added. Grains dissolved in a Parr bomb for 60-72 hours, were dried, and then converted to nitrates overnight. Once in nitrate form, samples were dried and brought up in 3 N HNO_3 and put through the ion exchange chromatography procedure listed in Table 1.

Smaller glass fragments that were optically free of zircons were picked and dissolved in ~250 µL of concentrated HF and a weighed drop (~0.007 g) of KU-229-235 on a hot plate overnight at ~150 C. Once dissolved, aliquots were pipetted into new, clean beakers leaving any residual zircon sediment at the bottom. The aliquots were then dried and re-dissolved in concentrated HNO_3, dried again and finally dissolved in the 3N HNO_3 loading solution. Then the glass aliquots were run through the column procedure in Table 1.

Isotopic dilution inductively coupled plasma mass spectrometry (ID-ICPMS) analyses:

Instrumentation:

U and Th isotopic analyses were made on a ThermoFisher Element 2 with a sector-field magnet and a single MasCom secondary electron multiplier (SEM). The ICPMS was operated in low mass resolution and in electrostatic peak jumping mode where the magnetic field was fixed, and an electric field hopped through the desired masses. Electrostatic scanning was used because of the short settling time compared to a magnet jump. Masses 229, 232, 235, and 238 were analyzed. Radio frequency (RF) power was set between 1018 and 1071 W. The flow rate for the Ar auxiliary gas was 0.90-0.96 L/min and the sample gas was 1.045-1.078 L/min, depending on tuning conditions of the analytical session.

Samples were introduced using a wet introduction system. An ESI PC3 spray chamber and ESI SC-E2 autosampler were used to uptake samples at ~200 μL/min. A platinum guard electrode (GE) was used, which increased sensitivity by an order of magnitude. For a 1 ppb U tuning solution, ~ 2 million cps of ^{238}U were detected with a sample uptake rate of ~200 μL/min. The sensitivity was about 60 mV/ppb (10^{11} Ω amplifier equivalent) for U. The dead time for the SEM detector was set at 4 ns.

Data acquisition:

KU 66-112 was used as a standard to monitor mass fractionation over each run. CRM 112a, the source of U in this solution, has a precisely determined $^{238}U/^{235}U$ ratio (Condon et al., 2010). A community Th isotopic standard has not been mixed or absolutely calibrated, and Th is close in mass to U, so we assumed Th mass fractionation would mimic U. All mass fractionation was normalized to the $^{238}U/^{235}U$ of CRM 112a using the exponential mass fractionation equation of Russell et al. (1978).

Measurement times were equal for all masses measured: the segment duration was 8 ms and the sample time was 2 ms for 3 passes and 600 runs. The settling time between each mass was 1 ms to remove any noise even though the electrostatic analyzer does not have a settling time. To minimize any oxide production, the percentage of UO_2 relative to ^{238}U was kept at 4 - 5.5 % in daily tuning.

RESULTS

This study has developed a method to determine the effects of realistic crystallization conditions (temperature, oxygen fugacity, and melt composition) on Th-U partitioning between synthetic zircon crystals and the residual melt. We define a zircon Th/U mineral/melt fraction factor $f = D_{Th}/D_U$. This ratio can be directly substituted into equation (2) used for the ^{230}Th correction and can potentially provide a more accurate and precise ^{230}Th correction if D_{Th}/D_U is determined precisely (~ 5%) using ID-ICPMS. We can determine this ratio to a higher precision than determining the individual partition coefficients because we can avoid the relatively imprecise concentration estimations involved in calculating partition coefficients. However, for the purposes of understanding the behaviors of U and Th individually under different temperatures, melt compositions, and oxygen fugacities, we have also reported individual partition coefficients from SIMS and EMPA measurements.

Experimental Petrology

Experimental run products:

Experiment textures were analyzed using cathodoluminescence (CL) and back-scatter electron (BSE) imaging. For each experiment, glass created by quenching the melt made up > 90 volume percent. Zircons were generally euhedral and varied in size from 5 μm to 100 μm wide with an average around 20 μm (Fig. 3). Larger crystals (> 20 μm) were preferentially sampled over smaller crystals for easier manipulation and to provide enough sample for precise analyses. No relationship was observed between crystal size and f (Fig. 6a, b).

For glass analyses, spots were placed both near grain boundaries and far from grain boundaries to check for any variation in f, D_{Th}, or D_U. Luo and Ayers (2009) had observed CL-dark ~ 1 μm wide rims around some of their zircons in the glass in BSE images that they

concluded were diffusive boundary layers. The layers they observed were too small to analyze and resolve a change in D_{Th} or D_U. We did not notice diffusive boundary layers in the glass around zircon crystals in BSE or CL images of any of our experiments. Our EMPA beam size was ~ 3 μm, so we could not directly measure ~ 1 μm around the zircon where Luo and Ayers (2009) observed diffusive boundary layers. However, SIMS and EMPA spots placed near grain boundaries did not observe a significant change in f, D_{Th}, or D_U in the glass.

Glass separates:

Melt compositions ranged from basaltic to andesitic (Table 2). Between 65% and 99% of the volume of each experiment consisted of glass. Analytical totals, measured by electron microprobe analyzer (EMPA), for experiment run product glasses are between 99 and 100 %, indicating that the melts were dry as intended. Glass in each sample was homogenous as indicated by the low variability across multiple analyses.

Zircon separates:

All experiments were performed at one atmosphere with the goal of producing zircon crystals with measurable U and Th concentrations. Zircon ranged from 5 to 100 μm in diameter with an average around 20 μm. Crystals were usually euhedral, indicating they did not grow on a preexisting nucleation seed. There was no difference in morphology across experiments with different f_{O2} or temperature, though morphology did change with differing Zr contents. Morphologies were also generally blocky, similar to the grains seen in Hanchar et al. (2001), which were also doped with higher concentrations of REE (Fig. 3).

In larger zircons (> 20 μm), sector zoning was apparent in several CL-imaged grains (Fig. 3, 6). Sector zoning may also be present in smaller zircons but was unable to be resolved. Light and dark zones were large enough in crystals > 20 μm to be analyzed separately using 3 μm

EMPA spots. CL-dark zones typically had higher D_{Th}, D_U, and D_{Th}/D_U (f) than CL-bright zones (Table 7). To precisely measure the variation in the D_{Th}/D_U (f) ratio between whole crystals, we employed isotope dilution methods, as commonly used by the U-Pb zircon geochronology community.

We also observed blocky morphologies similar to the zircons grown by Hanchar et al. (2001) who suggest that these habits are associated with high REE contents in crystals (Hanchar et al., 2001). Our crystals, doped with up to 1400 ppm Th and 1000 ppm U, had high concentrations of these elements relative to natural zircon, though concentrations of these elements in natural samples vary (e.g. Ickert et al., 2015, Hartmann and Santos, 2004). Concentrations were low enough that U and Th behavior could be approximated with Henry's law. The high concentrations of U and Th were useful in determining the D_{Th}, D_U, and D_{Th}/D_U at our intended precision (~ 5% analytical uncertainty).

Isotope Dilution Analyses

Gravimetric solution Th/U ratio:

The $^{232}Th/^{238}U$ of the gravimetric solution needed to be precisely measured and its Th and U isotopic compositions known to correct for mass fractionation and inversely calculate the spike $^{235}U/^{229}Th$ ratio. We corrected for air buoyancy using air pressure, humidity, and temperature during the weighing and for small quantities of ^{232}Th in CRM112a and ^{238}U in CRM66-7 by using previously determined impurity measurements (NBL, 2008; Condon et al., 2010). We estimate the $^{232}Th/^{238}U$ to be 2.11932 ± 0.00011, 2σ (Table 4). The relative uncertainty of ~52 ppm sets a limit on the systematic uncertainty of our measurements and provides first-principles traceability to the SI system (e.g., Condon et al, 2015).

Tracer calibration:

To attain the precision and accuracy required for improve ^{230}Th corrections for ^{206}Pb/^{238}U dates, we employed isotope dilution methods, which required mixing and calibrating a tracer artificially enriched in isotopes of both U and Th. We measured 12 aliquots of the ^{229}Th-^{235}U tracer mixed with the gravimetric solution. Tracer analyses produced a weighted mean ^{235}U/^{229}Th of 1.7893 and 2σ uncertainty of 0.0048 (Table 5). This tracer was then used to perform all following ID-ICP-MS analyses.

ID-ICP-MS analyses:

About 15 individual zircon grains and ~ 5 glass fragments were analyzed from each of six experimental runs from the Washington University experiments (Table 1). Individual grains and glass fragments were analyzed to understand whole-crystal D_{Th}/D_U (f) variation, mimicking the process of ID-TIMS, since the ^{230}Th correction makes up a large portion of the uncertainty budget for Cenozoic zircon dates measured using those methods. For each sample, f was calculated using the following equation.

$$f = \frac{(\ ^{232}Th\ /\ ^{238}U)_{zircon}}{(\ ^{232}Th/\ ^{238}U)_{glass}} = \frac{D_{Th}}{D_U},$$

An f was calculated for each of the ~15 zircon samples by averaging the ~5 glass ^{232}Th/^{238}U ratios since these measurements were within uncertainty of one another and expected to approach the same value. We propagated uncertainties from measurements, blank estimations, and spike calibration. Relative uncertainties across samples ranged from 1-5%. This precision revealed resolvable differences between individual crystals, which we attribute to the sector zoning observed in CL images and the different volumes of light and dark sectors. D_{Th}, D_U, and D_{Th}/D_U (f) variation between sectors was analyzed using SIMS and EMPA spot analyses (Fig. 4, Table 7).

SIMS analyses:

For SIMS zircon and glass measurements (Table 7), uncertainties were propagated from analytical uncertainties in measured isotope ratios as well as the internal reproducibility, estimated from repeat analyses of the 91500 zircon megacryst and NIST 610 glass Th/U ratios. Measured SIMS f values are within one standard deviation of the ID-ICPMS average for each sample (Fig. 4, Appendix B, Appendix C). The range of ID-ICPMS data is larger than the range of SIMS data except in the case of experiment J089, a basaltic andesite run at QFM-4. One J089 f value is higher than all the other data points but still within 1σ of the Burnham and Berry (2012) data produced under similar conditions (Appendix C). This SIMS analysis may have intersected adhering glass since this measurement had lower ZrO count rates than the other J089 zircon spots and higher count rates of ThO. Intersecting glass would raise the estimated f value since much of the total Th added to each experiment remains in the glass. This measurement was excluded from Fig. 4. SIMS analyses measured the U and Th variation between individual sectors, while ID-ICPMS analyses averaged partitioning behavior in the whole crystal.

Variation in D_{Th}/D_U:

D_{Th}/D_U (f) values range from ~0.4 to ~1.9 across all samples and all analyses (Fig. 4). Most samples have f values below 1, but under more oxidizing conditions (e.g. experiment H109, Fig. 4), these values can approach 1.5 – 2 and variability between grains increases. Under oxidizing conditions, U oxidizes to U^{6+} and is expected to be less compatible in the crystal. Under more reducing conditions, U forms the U^{4+} cation and is more compatible in the crystal.

Oxygen fugacity:

Samples H109, H110, and J089 are basaltic andesites from the same starting material that were grown under different f_{O2} conditions ranging from QFM + 4 to QFM - 4 (Fig. 4). D_{Th}/D_U values from these samples are well within 2σ of, but far more precise than, the D_{Th}/D_U (f)

calculated from Burnham and Berry (2012) measurements under similar conditions (Fig. 4). Burnham and Berry grew zircons of ~20 to 100 μm at ~1300º C in andesitic melts. Within each sample in Fig. 4, we resolve variation between individual crystal analyses. D_{Th}/D_U (f) decreases under more reducing conditions (Fig 4 b and c), which is in agreement with the observation by Burnham and Berry (2012).

Temperature and melt composition:

Synthesized samples were grown at temperatures ranging from 1410 to 1225º C with cooling rates ranging from 2 to 10 C/hr (Table 2, 3). In the basaltic andesite samples, doped with 1000 ppm of Th and U (J089, H099, H109, H110) zircon was grown by cooling from 1325 to 1225º C with 10º C/hr cooling rates. In the two andesite samples, zircon was grown by cooling from 1400 to 1325º C with a 10º C/hr cooling rate (J096) and from 1410 to 1350º C with a cooling rate of 2º C/hr (H092). D_{Th}/D_U (f) for these samples generally increased with increasing temperature, though these observations are not independent of changes in melt composition since andesites were synthesized at higher temperatures than the basaltic andesites (Fig. 5, Table 2, 3).

The M-value (Watson and Harrison, 1983) for basaltic andesites was 2.81 and andesites was 2.0 (Table 2). The M-value represents the ratio of network-modifiers to -formers and inverse silica activity. Zirconium oxide concentrations were between 5 and 7 wt% for all experiments. The high concentrations of Zr were necessary to saturate zircon at the temperatures (1225 - 1340º C) used in this study (Watson and Harrison, 1983).

In Fig. 5, the data from Rubatto and Hermann (2007) shows an increase in D_{Th}/D_U with temperature. Weighted means from our samples have higher D_{Th}/D_U, but D_{Th}/D_U from andesitic sample (H092) decreases compared to the two basaltic andesite experiments (H110, H099) (Fig. 5). H110, H099, and H092 were all grown under the same f_{O2} conditions (QFM). Data from Luo

and Ayers (2009) have large uncertainties and do not expose any correlations with T (Fig. 5). There is a decrease in D_{Th}/D_U between basaltic andesitic and andesitic experiments with increasing temperature that would otherwise have been contained within the uncertainties of Rubatto and Hermann (2007) or Luo and Ayers (2009) data. The magnitude of DTh/DU decrease from the basaltic andesites (H099, H110) to the andesite (H092) is less than the magnitude of D_{Th}/D_U increase with temperature implying that melt composition has the smallest effect on D_{Th}/D_U out of the parameters (oxygen fugacity, temperature, melt composition) analyzed in this study.

Sector zoning in zircon:

Many of the samples with larger zircons (> 20 μm) exhibit c-axis parallel sector zoning patterns (Fig. 3 a, b). Others show seemingly more unique zoning patterns, that are the result of the crystal c-axes non-parallel to the grain mount (Fig. 3c, d). Much of the variation in zoning patterns can be attributed to grain orientation on the different mounts. Regardless of orientation, EMPA and SIMS measurements were able to measure differences in D_U, D_{Th}, and D_{Th}/D_U (f) in light and dark sectors as shown in Table 7. Light zones had lower D_{Th}/D_U than dark zones in all experiments. For whole grain analyses, the volume proportion of light to dark sectors heavily influences the DTh/DU. In Fig. 5a, a H110 crystal with a larger proportion of light sectors would be expected to yield a whole crystal D_{Th}/D_U that is lower than another H110 crystal with a higher volume of dark sectors. Other zoning patterns are difficult to discern in CL images and not as commonly found in experiments. Measuring the change in D_{Th}/D_U in light and dark sector zones helps explain the variation in whole-grain analyses in Fig. 4 and 5.

We next discuss the inter-sample variation and the intra-crystal variation observed. The oxygen fugacity most significantly varies D_{Th}, D_U, and the D_{Th}/D_U ratio. We also suggest that

growth rates, melt advection, and disequilibrium crystallization should affect U and Th partitioning as the crystal is growing.

DISCUSSION

Our results show that varying the oxygen fugacity, melt composition, and temperature change way that U and Th partition between zircon and the coexisting melt (Fig. 4, 5). Oxygen fugacity appears to have the largest control on D_{Th}/D_U, with values ranging from ~0.4 to ~2 (Fig. 4). Temperature and composition have a lesser effect with D_{Th}/D_U shifting by only ~0.4 between the two parameters (Fig. 5). We also observe intra-crystal variation that we hypothesize results from different partitioning behaviors in the sector zones that were observed in cathodoluminescence (CL) images (Fig. 3, 6). Sector zoning is the result of disequilibrium crystallization, which is related to the growth rate of the crystal and diffusion of elements in the crystal structure and the melt. Intra-crystal variation in U and Th partitioning behavior adds complexity to assigning a whole crystal D_{Th}/D_U for the ^{230}Th correction. This can be remedied by estimating the relative volume of light and dark sectors to find an average D_{Th}/D_U for the whole crystal. Using the experimental data presented here, it is possible to improve the accuracy of D_{Th}/D_U estimates of natural samples based on knowledge of their oxygen fugacity, temperature, and composition.

Trends in D_{Th}, D_U, and D_{Th}/D_U

Variation between SIMS and ID-ICPMS measurements

Measurements of D_{Th}/D_U by SIMS and ID-ICPMS varied both among zircons from each sample and between the two methods (Fig. 4), although the range of values from each method generally overlap. SIMS analyses were calibrated by applying corrections to unknowns based on the discrepancy between measured spots on a shard of the zircon megacryst 91500 and the $^{232}Th/^{238}U$ ratio reported by Weidenbeck et al. (1995). The accuracy of our ID-ICPMS methods was verified by measuring the Th/U ratio of 91500 (Wiedenbeck et al., 1995). These results and

the weighted mean appear in Table 6 along with the Wiedenbeck et al. (1995) weighted mean Th/U ratio. Our $^{232}Th/^{238}U$ ratios agree within 2σ analytical uncertainty of the Wiedenbeck et al. (1995) results (Table 6). Accurate calibration of our ID-ICPMS methods precludes analytical bias as the source of the discrepancy between the ID-ICPMS and SIMS analyses. The discrepancy can instead be explained by the fact that SIMS methods are in situ, ID-ICPMS methods dissolve the whole grain, and therefore any intra-grain heterogeneity will cause some scatter.

Though the majority of ID-ICPMS grain analyses lie within the range of SIMS and EMPA data points, which are expected to represent the extreme values of D_{Th}/D_U, there are a few outliers in experiment H110 (Fig. 4). We propose a few hypotheses explaining the higher D_{Th}/D_U. First, when leaching the analyzed grains in cold HF, some of the glass may not have been completely removed from the grain. Since more Th remains in the glass, analyzing adhered glass would result in an artificially elevated D_{Th}/D_U. Second, since we selected a small subset of the total grain population in each experiment, it is possible that we did not sample the entire range of D_{Th}/D_U values with SIMS and EMPA. Third, it is possible that we did not completely dissolve the entire zircon grain before analysis, which would skew results. We suggest that the first or second hypotheses are the most likely culprits since grains were left to dissolve for ~ 60 hours in a Parr time, which is sufficient time for zircons to dissolve. The majority of the heterogeneity between analyses can be explained by differences in partitioning behavior between analyzed light and dark sectors, it is likely an alternative mechanism affected the two Th-enriched outliers in experiment H110.

Inter-experiment variation of U and Th partitioning

Incorporation of Th and U is controlled by temperature, pressure, melt composition, growth rate, interface kinetics at the crystal face, and the relative compatibility of these elements at different crystal faces. Overall, oxygen fugacity was observed to have the largest influence on partitioning behavior in zircon crystals, while temperature and melt composition had less obvious effects between each experiment.

Oxygen fugacity

D_U generally decreases with increasing oxygen fugacity, while the D_{Th} data do not reveal an obvious pattern in both light and dark sectors (Table 7). Our EMPA data sampled much smaller spot sizes (3 μm) than the SIMS (~ 20 μm), so we can observe general patterns in D_U and D_{Th} behavior within and between sectors (Fig. 6). We have primarily compared D_{Th}/D_U data because the ratio can be used for the ^{230}Th correction and the ID-ICP-MS measurements of the ratio is much more precise than individual D_{Th} and D_U measurements.

Compared to D_{Th}/D_U ratios from Burnham and Berry (2012), our data were collected with much lower uncertainties. Our results show that the magnitude of D_{Th}/D_U change over the QFM-4 to QFM+4 oxygen fugacity range is much smaller than previously determined by Burnham and Berry (2012) (Fig. 6). These results reveal more intra-crystal variation at QFM and QFM+4 conditions. At QFM+4, our whole-crystal D_{Th}/D_U analyses vary by ~ 0.8, and at QFM, our results vary by ~ 1. At QFM-4, most analyzed crystals yield data within uncertainty of each other. All data cluster around a D_{Th}/D_U of ~ 0.5 (Fig. 6).

The oxygen fugacity range in this study (QFM +4 to QFM -4) covers typical f_{O2} ranges from the upper mantle (< 400 km) to the upper continental crust (McCammon 2005). McCammon (2005) suggested typical continental crust oxygen fugacities of QFM-2 to QFM+5

and upper mantle f_{O2} values from QFM-4 to QFM+2. Oxygen fugacity represents the 'availability' of oxygen and controls the oxidation states of elements in a system. In geologic settings, U^{4+} and U^{6+} are the most common oxidation state of U (Burns, 1999). At higher oxygen fugacities, where U^{6+} is a more frequent species than at lower f_{O2}, we expect a lower D_U and higher D_{Th}/D_U. The higher ratio suggests that U is less preferentially partitioned into the crystal than at lower oxygen fugacities because U^{6+} does not partition into the crystal structure and thus remains in the melt.

Burnham and Berry (2012) hypothesized that the gradual decrease in D_U with increasing f_{O2} suggested U^{4+} oxidized to U^{5+} before U^{6+}. Since the D_U did not decrease stepwise, they suggested that U^{4+} could not oxidize directly to U^{6+}. This behavior could also be explained by oxidation of only some U^{4+} to U^{6+} ions over the oxygen fugacity range. The oxidation of U ions could increase asymptotically with increasing f_{O2}, which would cause the D_U to asymptotically decrease.

Burnham and Berry (2012) measured a D_{Th} of 1.19 ± 1.34 (2σ) using SIMS over an oxygen fugacity range of QFM-7.7 to QFM+6.6. We also do not see significant variation in D_{Th} with changing oxygen fugacity (QFM -4 to QFM+4). D_{Th} likely does not vary systematically with f_{O2} because it does not exist at an oxidation state higher than Th^{4+}. In our experiments, as f_{O2} increased (QFM+2 to QFM+4), D_{Th}/D_U approached unity meaning that U and Th have equal partitioning behavior (Fig. 4). Mass balance calculations from Krawczynski et al. (in prep) suggest that U^{6+} did not volatilize out of the system as hypothesized by Burnham and Berry (2012) and Schreiber (1983).

Temperature and composition

With increasing temperature and increasing silica content in the melt composition D_{Th} and D_U decrease (Table 7). Rubatto and Hermann (2007) found that D_U and D_{Th} both decrease with increasing temperature at 2 Gpa. Luo and Ayers (2009) report D_U and D_{Th} over a range of temperatures (800 - 1300°C) and pressures (0.1 - 1.5 GPa). When comparing the D_{Th}/D_U ratios in both studies, D_{Th}/D_U increases with temperature (Fig. 5).

Compared to our data, D_{Th}/D_U ratios from Rubatto and Hermann (2007) are lower over the lower temperature range, agreeing with their conclusions. Over the temperature range shown in Fig. 5b, D_{Th}/D_U ratios from Rubatto and Hermann (2007) and this study range from ~0.2 to ~0.8, which is smaller than the range of f values in the oxygen fugacity series. The variation in D_{Th}/D_U is even smaller (~0.05 to 0.6) in the Rubatto and Hermann (2007) dataset, which was conducted over the more realistic temperature range of 800 to 1050 C. This suggests that temperature has a lesser influence on f values than f_{O2}.

Our experiments had basaltic andesitic and andesitic melt compositions (Table 2). Experiments with andesitic melts had to be synthesized at higher temperatures, so temperature and melt composition are coupled. Since these two parameters are coupled, we cannot definitively determine the effect of each. In Fig. 5, the D_{Th}/D_U of H092 drops below the D_{Th}/D_U of the two basaltic andesites (H099 and H110). These three experiments were grown under the same f_{O2} conditions (QFM), so oxygen fugacity should not affect the f values. Since we expect D_{Th}/D_U to increase with temperature, the change in melt composition could be the cause of the decrease in D_{Th}/D_U between the weighted means of the basaltic andesites and andesite samples (Fig. 5). Within each sample there is discrepancy between individual measurements in all EMPA, SIMS, and ID-ICPMS data (Fig. 6, Table 7). These have been interpreted to be the result

of different volume proportions of CL light and dark sectors, each with different U and Th partitioning behavior (Appendix C, Table 7, Fig. 6).

Disequilibrium growth processes and expressions

The combination of growth conditions and disequilibrium growth processes appears to control the variation in D_{Th}/D_U for zircon crystals. Growth rates are a first order control on disequilibrium processes. The timescales of zircon growth could affect the ability of U and Th to diffuse fast enough through the melt to be incorporated into the crystal (e.g. Watson 1996), or advection of the melt could resupply these elements to the crystal-melt interface regularly.

Another control on U and Th incorporation into the zircon crystals includes sector zoning, as observed in CL images (Fig. 3, 6). Sector zoning is the expression of preferential partitioning at different crystal faces, which can be related to growth rate as hypothesized by Paterson and Stephens (1992), Watson and Liang (1995), and Vavra et al., (1996). Models by Shimizu (1978, 1983) predict the relative concentrations of both compatible and incompatible elements within each sector. All of these hypotheses and observations help explain the complexity of U and Th behaviors observed in our whole crystal and spot analyses. Understanding the variability in our data can help provide a better range of D_{Th}/D_U for the ^{230}Th correction.

Zircon saturation, nucleation, and growth rate

To hypothesize how D_{Th}, D_U, and D_{Th}/D_U can vary between CL-bright and -dark sectors of a crystal, we must consider how zircon saturation, nucleation, and growth rates affect trace element partitioning. Zircon saturation depends on temperature and melt composition, especially the concentration of Zr in the melt. Zircon can crystallize in melt compositions ranging from basaltic to rhyolitic (Watson and Harrison, 1983), but mafic melts require high Zr concentrations

(> 5000 ppm), which are only possible in late-stage, evolved melts (Boehnke et al., 2013). Growth rates are thought to be limited by Zr delivery to the mineral-melt interface (e.g. Watson, 1996). But advection of the melt could increase growth rates, accounting for the faster growth seen in experimental studies and some natural crystals. Faster growth rates could, in turn, cause deviation from equilibrium trace element partitioning.

Watson (1996) calculated three-dimensional growth rates for zircon in granitic melts with 3 wt% water under different temperature regimes including constant temperature and linearly time dependent temperature. Watson assumed that the melt is physically static and that zircon growth is influenced exclusively by diffusion of species in the melt. For the three-dimensional spherical model, growth rates for zircon > 30 μm fell between 10^{-13}-10^{-17} cm/s over the 850-650 ºC range.

Watson (1996) argued that melt stirring during zircon crystallization was unimportant to the growth behavior except under instances of extreme shearing, and only Zr diffusion affected growth rates. Advection could occur due to new magmatic input to the system, in the case of an evolving volcanic center, or due to advection within the melt of an experimental charge. In either case, advection would change the availability of Zr within the system, increasing the instantaneous growth rate for a zircon crystal. While diffusion heavily influences zircon growth rates as shown by Watson (1996) and Watson and Harrison (1983), advection could also play an important role by refreshing the supply of Zr near the crystal.

Schmitt et al. (2011) calculated zircon growth rates for Late Pleistocene zircon in the Acigöl rhyolite field (Central Anatolia, Turkey) using core and rim (U-Th)/He eruption ages. By subtracting the rim age from the core age, they calculated zircon crystallization timescales of

about 6-8 kyr. For a typical 50 μm-radius crystal, they calculated growth rates of approximately 3×10^{-14} cm/s, within the range provided by Watson (1996) for diffusion-controlled growth.

The average growth rate calculated by Schmitt et al (2011) described the slowest growth possible to produce a 50 μm-radius crystal. An instantaneous growth rate could operate faster with hiatuses throughout the growth period to produce the same average growth rate. Thus, the average growth rate describes the minimum growth rate for the system. This implies that some zircons in the system could grow at much faster rates and do not require constant growth. Non-constant growth rates and interface kinetics can result in compositional zoning, such as sector zoning.

Sector zoning:

To explain variation between D_{Th}, D_U, and D_{Th}/D_U in each crystal, we investigate the degree to which fast growth rates and melt advection affect compositional zoning in zircon crystals. Observable zoning in cathodoluminescence (CL) imaging is usually the result of variation in REE composition (e.g. Hanchar et al., 2001), and changing Hf concentrations in BSE images (e.g. Cherniak et al., 1997). Sector zoning and oscillatory zoning have been observed in many zircon populations with both types of zoning sometimes occurring in the same crystal (Cofu et al., 2003). Zoning was frequently observed on micron and sub-micron scales in zircon (e.g. Patterson and Stephens, 1992, Hanchar et al., 2001, Corfu et al., 2003), and is produced by disequilibrium crystallization. The relationships between crystal-melt interface kinetics, changing melt composition, crystal growth rate, and lattice and melt diffusivity that control the disequilibrium crystallization which produces sector zoning are debated.

Sector zoning is thought to be related to kinetic factors and rapid changes in growth environment, roughness of the growth surface coupled with changes in growth rate, or the

relationship between lattice diffusivity and growth rate. Paterson and Stephens (1992) interpreted that sector zoning in titanite crystals was the morphological outcome of kinetic factors and rapid changes in growth environment (Paterson and Stephens, 1992). They argued against a slow lattice diffusivity mechanism since such a mechanism would not be able to produce the sharp zoning patterns indicative of sector zoning but would rather produce a gradational change in element concentration.

Different from Paterson and Stephens (1992), Vavra et al. (1996) attributed sector zoning to rapid changes in growth rate related to the morphology of growing crystal face. They interpreted that rougher crystal faces would have more rapid growth rates than smoother faces. Close to the roughening transition, crystal faces would switch back and forth from smooth to rough causing abrupt changes in growth rate. This rapidly fluctuating growth rate related to the roughness of the growth surface contributed to sector zoning. Saturation of the growth medium added another component to this interpretation. Crystal faces become rougher with increasing temperature and supersaturation of the growth medium. Evidence for this mechanism comes from their observation that planar growth banding occurred along smoother surfaces away from the converging sectors. The converging sectors represent the boundaries between faces of differing roughness and melt saturation.

Watson and Liang (1995) proposed a hypothesis more closely related to that of Paterson and Stephens (1992). They suggested that lattice diffusivity alone is unable to produce sector zoning. They hypothesized that sector zoning is caused by the relationship between growth rate (V) and lattice diffusivity (D_i) for zoned element *i*. They concluded that at some value of the dimensionless parameter Vl/D_i, where *l* is the thickness of the enriched surface-growth layer, compositional sector zoning was inevitable for element *i* in a crystal that selectively enriches *i* on

different crystal faces. If lattice diffusivity is sufficiently slow, a significantly faster growth rate can produce sharp sector zones.

Watson and Liang (1995) calculated reasonable geologic growth rates for zircon to be 10^{-19} - 10^{-18} m/s at 700 °C. According to their calculations, lattice diffusivities (D_i) would need to be slower than 10^{-27} - 10^{-28} m^2/s for tetravalent cations in zircon to produce sector zoning. They reported lattice diffusivities for REE diffusion in zircon crystals to be approximately 10^{-34} m^2/s, which is slow enough to produce sector zoning. Later, Cherniak et al. (1997) suggested that compositional sector zoning is unavoidable except under the most extreme temperature conditions due to the slow lattice diffusivities of tetravalent cations, agreeing with Watson and Liang (1995).

Other studies observed sector zoning related to REE concentrations. Hanchar et al. (2001) found that as REE concentration increased, crystals became blockier as growth on the {110} and {010} faces is slowed. They also found that sector zoning became more pronounced in crystals doped with MREE and HREE. Zones reflected differences in REE concentration in their synthetic crystals. They suggested that various sectors may accommodate REE incorporation differently, which meant that partition coefficients differed for each crystal face. Their synthetic crystals contained both sector and oscillatory zones, which they interpreted as evidence that different sectors grew simultaneously, potentially at different growth rates and with changing REE composition in the melt.

Based on the equations derived by Shimizu (1978, 1983), we expected the concentration of incompatible elements to increase asymptotically from the equilibrium partitioning behavior as these elements increased in concentration in the melt surrounding the crystal. For compatible elements, the ratio of the concentration in the solid to the original concentration was expected to

decrease. Two EMPA spots in a CL-bright sector in zircon A of the H110 experiment have U and Th partition coefficients that increase moving away from the crystal center (spots 1, 2 in zircon A, Fig. 6b). Since D_U and D_{Th} and therefore the concentrations of U and Th increase moving away from the center of the crystal, some mechanism must have replenished the supply of U and Th to the crystal as it was growing. This observation could be the result of melt advection. As the melt circulates, it could replenish the supply of U and Th to the crystal as it grows, which could cause the increase in DU and DTh observed in Fig. 6b. Growth rate and melt advection affect the incorporation of U and Th at different crystal faces, which could have caused the intra-crystal variation in D_{Th}, D_U, and D_{Th}/D_U within single experiments (Fig 6).

Observed variation between sectors

We observed noticeable variation in D_{Th}, D_U, and D_{Th}/D_U (f) in CL-bright and -dark sectors in all experiments. Dark sectors have higher and brighter sectors have lower D_{Th}, D_U, and D_{Th}/D_U. These results suggest that dark sectors have a higher capacity to incorporate U and Th into the lattice since dark sectors have much higher concentrations of Th and U (Table 7). The difference in partition coefficients between CL-bright and -dark sectors suggests that these zones were not in equilibrium with each other (Table 7). Sector zones could have formed by changing melt concentration of U and Th on different sides of the crystals that resulted in changes in partitioning behavior.

Implications for the ^{230}Th correction

Using D_{Th}/D_U from previous studies (e.g. Burnham and Berry, 2012, Luo and Ayers, 2009, Rubatto and Hermann, 2007) to correct for ^{230}Th intermediate daughter disequilibrium using equation (2) makes up the majority of the uncertainty budget for young zircon (e.g., up to 0.07% uncertainty at 66 Ma, up to 3% uncertainty at 1 Ma). Since zircon can be found in almost

any felsic rock, decreasing analytical uncertainty can enable workers to tackle a large variety of geologic questions-- from the intricacies of a caldera complex to the evolution of a basin. In particular, Cenozoic zircons can be useful when resolving complex geologic processes on millennial timescales because they have smaller absolute uncertainties. For instance, more precise $^{238}U/^{206}Pb$ ages would allow us to understand more rapid geologic processes, like incremental pluton assembly (e.g., at the Mount Princeton magmatic center; Mills and Coleman, 2013) or provenance studies (e.g., of tectonically active Quaternary shelf deposits such as the Magdelena Shelf off CA; Fletcher et al., 2007) to be better resolved.

We have observed in this study that CL-dark and -bright sector zones and different crystallization conditions can produce different D_U, D_{Th}, and D_{Th}/D_U. Usually, CL-bright zones occurred along the prismatic faces of the crystals while dark zones typically were found at the two pyramidal points (Fig 3a and b). Across all samples, the range of whole crystal f values exists between ~0.4 and 2, and the variation between CL-light and -dark sectors is ~0.3 to 2.5. This range of D_{Th}/D_U values from this study is much smaller than observed in previous studies (e.g. Rubatto and Hermann, 2007, Luo and Ayers, 2009, Burnham and Berry, 2012), which suggests that the range of f values for the ^{230}Th correction is probably smaller than previously expected. Since the largest D_{Th}/D_U variations are seen between samples produced at different f_{O2}, that parameter would be most useful to constrain the possible f values in natural samples. If higher precision is needed on the ^{230}Th correction, then estimating the volume ratio and applying D_{Th}/D_U ratios to specific CL-bright and -dark sectors is possible and would need to be coupled with oxygen fugacity, temperature, and melt composition estimates.

The variation in U and Th ratios that we observed in zircons within a single experiment is a common phenomenon observed in samples in U-series literature. When calculating a U-series

age for a system (e.g. to determine magma storage below a volcano, Stelten and Cooper, 2012) using an isochron requires a range of $^{238}U/^{232}Th$ ratios. $^{238}U/^{232}Th$ ratios from Stelten and Cooper (2012) range from 2 to 8 for zircons from the Rock Mesa and Devil's Hills rhyolites from the South Sister volcano. The range of these ratios is larger than we observe in our experimental data, but we do not know if or how U and Th partitioning could have varied as the Rock Mesa and Devil's Hills rhyolites crystallized and evolved (Stenton and Cooper, 2012). Natural zircons within the same rock are commonly found with varying Th/U ratios, so it follows that we also measured a range of Th/U ratios in our experiments.

To apply D_{Th}/D_U to a whole crystal U-Pb zircon date grown under similar conditions, we want to quantify an average ratio to represent partitioning behavior for the entire crystal. Since D_{Th}/D_U varies across sectors, we need to estimate the relative volume of light and dark sectors in a zircon crystal. To estimate relative sector volume for a natural zircon crystal with a c-axis that is approximately twice as long as the a and b axes, the ratio of light sectors along the prism faces to dark sectors at the points would be ~0.6. This ratio can then be used to calculate an average D_{Th}/D_U for the whole grain from our experimental data. Since we do not have any experiments grown in rhyolitic melt compositions, we cannot confidently extrapolate D_{Th}/D_U ratios to natural zircons grown in rhyolitic or granitic melts. To estimate oxygen fugacity conditions during crystallization of natural zircon, cerium and europium anomalies are useful (e.g. Smythe and Brenan, 2016). Temperature can be estimated measuring Ti in zircon (e.g. Watson et al., 2006), and composition is determined by bulk rock chemistry. Using these proxies would obtain the highest possible precision to estimate the D_{Th}/D_U ratios.

D_{Th}/D_U ratios in the experiments of this range from ~0.4 to 2. In most natural samples, we find that D_{Th}/D_U does not exceed 1, meaning that zircon usually crystallizes with a ^{230}Th

deficit (e.g. Schärer, 1984, Crowley et al., 2007). Our oxygen fugacity conditions range from QFM-4 which would be found at upper mantle conditions and QFM+4 which would be found within the continental crust, but not at the temperatures or compositions of our experiments (McCammon, 2005). We could find mid-ocean ridge basalts with f_{O2} conditions of approximately QFM+0, which would crystalize at similar temperatures and basaltic melt compositions. This would be the best direct application of our experimental values since H110 is a basaltic andesite experiment run at QFM+0. H110 has a weighted mean D_{Th}/D_U of 0.7388 (Table 7), which agrees with the observation that most zircon preferentially exclude Th. The oxygen fugacities in this study exceed the range where we would expect to typically find upper crustal zircon (~ QFM-2 to QFM+5, McCammon, 2005) to understand the overall patterns of Th and U partitioning between zircon crystals and melts. With a larger range of melt compositions and temperatures covered in these experiments, we can apply D_{Th}/D_U ratios to a wider variety of natural conditions.

While we have only covered a small range of natural conditions, we have observed the significance that sector zoning plays in Th and U partitioning. This insight can help future studies apply D_{Th}/D_U values to partial or whole crystal analyses and help understand the complexity of Th and U partitioning behavior as it relates to melt conditions including temperature, oxygen fugacity, melt composition, growth rate, and sector zoning.

CONCLUSIONS

We show that it is possible to synthesize zircons doped with U and Th that are large enough to successfully analyze using in situ (EMPA and SIMS) and bulk crystal (ID-ICPMS) methods. Newly developed ID-ICPMS methods quantitatively separate U and Th from

experimental zircons using a low-volume, low-blank procedure and achieve ~1-5 % (2σ) analytical uncertainty.

We observe sector zoning in CL images of synthetic zircons, which we argue is the source of statistically significant and previously unobserved variation in measured D_{Th}/D_U. CL-dark zones have a consistently higher D_{Th}/D_U than CL-bright zones by a factor of ~2.

Despite the intra- and inter-grain variability in measured D_{Th}/D_U, there are significant trends in D_{Th}/D_U partitioning as a function of magma system parameters. Oxygen fugacity, temperature, and melt composition all affect the D_{Th}/D_U ratio. Consistent with, but smaller in magnitude than the results of Burnham and Berry (2012), f_{O2} has the largest effect on relative Th/U partitioning in zircon, and therefore is an important parameter to constrain if making ^{230}Th disequilibrium corrections in zircon using D_{Th}/D_U. The zircon mineral-melt D_{Th}/D_U measurements of this study can be used to inform ^{230}Th corrections for zircons in only a narrow range of natural conditions. However, the results, including quantifying the potential effects of sector zoning, can be used as a starting point for further experiments.

Future work should focus on understanding the effects of pressure and volatile content on D_{Th}/D_U, expanding these experiments to more evolved compositions that more frequently saturate zircon, and to lower temperatures. A more expansive dataset is required for experimental Th/U partitioning data to be used in routine U-Pb geochronology. However, extending the experimental parameter space and making zircon D_{Th}/D_U measurements with our high precision techniques has the potential to help explain variability in zircon Th/U and to reduce uncertainty on the ^{230}Th correction, leading to more precise and accurate $^{206}Pb/^{238}U$ dates for Cenozoic zircon.

REFERENCES

Boehnke, P., Watson, E. B., Trail, D., Harrison, T. M., & Schmitt, A. K. (2013). Zircon saturation re-revisited. *Chemical Geology*, *351*, 324-334.

Bourdon, B., Turner, S., Henderson, G. M., & Lundstrom, C. C. (2003). Introduction to U-series geochemistry. *Reviews in Mineralogy and Geochemistry*, *52*(1), 1-21.

Burnham, A. D., & Berry, A. J. (2012). An experimental study of trace element partitioning between zircon and melt as a function of oxygen fugacity. *Geochimica et Cosmochimica Acta*, *95*, 196-212.

Burns P. C. (1999) The Crystal Chemistry of Uranium. *Reviews in Mineralogy and Geochemistry*, *38*(1), 22-90.

Cheng, H., Edwards, R. L., Shen, C. C., Polyak, V. J., Asmerom, Y., Woodhead, J, Hellstrom, J., Wang, Y., Kong, X., Spötl, C. and Wang, X. (2013). Improvements in ^{230}Th dating, ^{230}Th and ^{234}U half-life values, and U-Th isotopic measurements by multi-collector inductively coupled plasma mass spectrometry. *Earth and Planetary Science Letters*, *371*, 82-91.

Cherniak, D. J., Hanchar, J. M., & Watson, E. B. (1997). Diffusion of tetravalent cations in zircon. *Contributions to Mineralogy and Petrology*, *127*(4), 383-390.

Cherniak, D. J., & Watson, E. B. (2001). Pb diffusion in zircon. *Chemical Geology*, *172*(1-2), 5-24.

Condon, D. J., McLean, N., Noble, S. R., & Bowring, S. A. (2010). Isotopic composition (238U/235U) of some commonly used uranium reference materials. *Geochimica et Cosmochimica Acta*, *74*(24), 7127-7143.

Corfu, F., Hanchar, J. M., Hoskin, P. W., & Kinny, P. (2003). Atlas of zircon textures. *Reviews in Mineralogy and Geochemistry*, *53*(1), 469-500.

Crowley, J. L., Schoene, B., & Bowring, S. A. (2007). U-Pb dating of zircon in the Bishop Tuff at the millennial scale. *Geology*, *35*(12), 1123-1126.

DeCelles, P. G., Carrapa, B., & Gehrels, G. E. (2007). Detrital zircon U-Pb ages provide provenance and chronostratigraphic information from Eocene synorogenic deposits in northwestern Argentina. *Geology*, *35*(4), 323-326.

Hanchar, J. M., Finch, R. J., Hoskin, P. W., Watson, E. B., Cherniak, D. J., & Mariano, A. N. (2001). Rare earth elements in synthetic zircon: Part 1. Synthesis, and rare earth element and phosphorus doping. *American Mineralogist, 86*(5-6), 667-680.

Harrison, T. M., & Watson, E. B. (1983). Kinetics of zircon dissolution and zirconium diffusion in granitic melts of variable water content. *Contributions to Mineralogy and Petrology*, *84*(1), 66-72.

Hartmann, L. A., & Santos, J. O. S. (2004). Predominance of high Th/U, magmatic zircon in Brazilian Shield sandstones. *Geology*, *32*(1), 73-76.

Heaman L. M. and Parrish R. R. (1991) U-Pb geochronology of accessory minerals. In Applications of Radiogenic Isotope Systems to Problems in Geology. Mineralogical Association of Canada Short Course Handbook 19 (eds. J. M. Heaman and J. N. Ludden). pp. 59–102.

Ickert, R. B., Mundil, R., Magee Jr, C. W., & Mulcahy, S. R. (2015). The U–Th–Pb systematics of zircon from the Bishop Tuff: a case study in challenges to high-precision Pb/U geochronology at the millennial scale. *Geochimica et Cosmochimica Acta*, *168*, 88-110.

Jaffey, A. H., Flynn, K. F., Glendenin, L. E., Bentley, W. T., & Essling, A. M. (1971). Precision measurement of half-lives and specific activities of U 235 and U 238. *Physical review C*, *4*(5), 1889.

Jochum, K.P., Weis, U., Stoll, B., Kuzmin, D., Yang, Q., Raczek, I., Jacob, D.E., Stracke, A., Birbaum, K., Frick, D.A. and Günther, D., (2011). Determination of reference values for NIST SRM 610–617 glasses following ISO guidelines. *Geostandards and Geoanalytical Research*, *35*(4), 397-429.

Lissenberg, C. J., Rioux, M., Shimizu, N., Bowring, S. A., & Mével, C. (2009). Zircon dating of oceanic crustal accretion. *Science*, *323*(5917), 1048-1050.

Luo, Y., & Ayers, J. C. (2009). Experimental measurements of zircon/melt trace-element partition coefficients. *Geochimica et Cosmochimica Acta*, *73*(12), 3656-3679.

Fletcher, J. M., Grove, M., Kimbrough, D., Lovera, O., & Gehrels, G. E. (2007). Ridge-trench interactions and the Neogene tectonic evolution of the Magdalena shelf and southern Gulf of California: Insights from detrital zircon U-Pb ages from the Magdalena fan and adjacent areas. *Geological Society of America Bulletin*, *119*(11-12), 1313-1336.

Mattinson, J. M. (1973). Anomalous isotopic composition of lead in young zircons. *Carnegie Institution of Washington Yearbook*, *72*, 613-616.

Mattinson, J. M. (2005). Zircon U–Pb chemical abrasion ("CA-TIMS") method: combined annealing and multi-step partial dissolution analysis for improved precision and accuracy of zircon ages. *Chemical Geology*, *220*(1-2), 47-66.

McCammon, C. (2005). The paradox of mantle redox. *Science*, *308*(5723), 807-808.

McLean, N. M., Bowring, J. F., & Bowring, S. A. (2011). An algorithm for U-Pb isotope dilution data reduction and uncertainty propagation. *Geochemistry, Geophysics, Geosystems*, *12*(6).

Mills, R. D., & Coleman, D. S. (2013). Temporal and chemical connections between plutons and ignimbrites from the Mount Princeton magmatic center. *Contributions to Mineralogy and Petrology*, *165*(5), 961-980.

Paterson, B. A., & Stephens, W. E. (1992). Kinetically induced compositional zoning in titanite: implications for accessory-phase/melt partitioning of trace elements. *Contributions to Mineralogy and Petrology*, *109*(3), 373-385.

Rubatto, D., & Hermann, J. (2007). Experimental zircon/melt and zircon/garnet trace element partitioning and implications for the geochronology of crustal rocks. *Chemical Geology*, *241*(1-2), 38-61.

Russell, W. A., Papanastassiou, D. A., & Tombrello, T. A. (1978). Ca isotope fractionation on the Earth and other solar system materials. *Geochimica et Cosmochimica Acta*, *42*(8), 1075-1090.

Schärer, U. (1984). The effect of initial ^{230}Th disequilibrium on young U-Pb ages: the Makalu case, Himalaya. *Earth and Planetary Science Letters*, *67*(2), 191-204.

Schmitt, A. K. (2011). Uranium series accessory crystal dating of magmatic processes. *Annual Review of Earth and Planetary Sciences*, *39*.

Schmitt, A. K., Danišík, M., Evans, N. J., Siebel, W., Kiemele, E., Aydin, F., & Harvey, J. C. (2011). Acigöl rhyolite field, Central Anatolia (part 1): high-resolution dating of eruption episodes and zircon growth rates. *Contributions to Mineralogy and Petrology*, *162*(6), 1215-1231.

Schoene, B. (2014). U–Th–Pb Geochronology. *Treatise on geochemistry*, *4*, 341-378.

Schoene, B., Samperton, K. M., Eddy, M. P., Keller, G., Adatte, T., Bowring, S. A., ... & Gertsch, B. (2015). U-Pb geochronology of the Deccan Traps and relation to the end-Cretaceous mass extinction. *Science*, *347*(6218), 182-184.

Schoene, B., Eddy, M. P., Samperton, K. M., Keller, C. B., Keller, G., Adatte, T., & Khadri, S. F. (2019). U-Pb constraints on pulsed eruption of the Deccan Traps across the end-Cretaceous mass extinction. Science, 363(6429), 862-866.

Schreiber H. D. (1983) The chemistry of uranium in glass-forming aluminosilicate melts. J. Less-Common Metals 91, 129–147.

Shimizu, N. (1978) Analysis of the zoned plagioclase of different magmatic environments: a preliminary ion-microprobe study. Earth and Planetary Science Letters 39, 398-406.

Shimizu, N. (1983) Interface kinetics and trace element distribution between phenocrysts and magma. In: Augustithis, S.S. (Ed.) The Significance of Trace Elements in Solving Petrogenetic Problems and Controversies. Theophrastus Publications, Athens, 175-195.

Smythe, D. J., & Brenan, J. M. (2016). Magmatic oxygen fugacity estimated using zircon-melt partitioning of cerium. *Earth and Planetary Science Letters*, *453*, 260-266.

Stelten, M. E., & Cooper, K. M. (2012). Constraints on the nature of the subvolcanic reservoir at South Sister volcano, Oregon from U-series dating combined with sub-crystal trace-element analysis of plagioclase and zircon. *Earth and Planetary Science Letters*, *313*, 1-11.

Tappa, M. J., Coleman, D. S., Mills, R. D., & Samperton, K. M. (2011). The plutonic record of a silicic ignimbrite from the Latir volcanic field, New Mexico. *Geochemistry, Geophysics, Geosystems*, *12*(10).

Tissot, F. L., & Dauphas, N. (2015). Uranium isotopic compositions of the crust and ocean: Age corrections, U budget and global extent of modern anoxia. *Geochimica et Cosmochimica Acta*, *167*, 113-143.

Vavra, G., Gebauer, D., Schmid, R., & Compston, W. (1996). Multiple zircon growth and recrystallization during polyphase Late Carboniferous to Triassic metamorphism in granulites of the Ivrea Zone (Southern Alps): an ion microprobe (SHRIMP) study. Contributions to Mineralogy and Petrology, 122(4), 337-358.

Watson, E. B. (1996). Dissolution, growth and survival of zircons during crustal fusion: kinetic principals, geological models and implications for isotopic inheritance. *Earth and Environmental Science Transactions of the Royal Society of Edinburgh*, *87*(1-2), 43-56.

Watson, E. B., Chemiak, D. J., Hanchar, J. M., Harrison, T. M., & Wark, D. A. (1997). The incorporation of Pb into zircon. *Chemical Geology*, *141*(1-2), 19-31.

Watson, E. B., & Harrison, T. M. (1983). Zircon saturation revisited: temperature and composition effects in a variety of crustal magma types. *Earth and Planetary Science Letters*, *64*(2), 295-304.

Watson, E. B., & Liang, Y. (1995). A simple model for sector zoning in slowly grown crystals: Implications for growth rate and lattice diffusion, with emphasis on accessory minerals in crustal rocks. American Mineralogist, 80(11-12), 1179-1187.

Watson, E. B., Wark, D. A., & Thomas, J. B. (2006). Crystallization thermometers for zircon and rutile. *Contributions to Mineralogy and Petrology*, *151*(4), 413.

Widmann, P., Davies, J. H. F. L., & Schaltegger, U. (2019). Calibrating chemical abrasion: Its effects on zircon crystal structure, chemical composition and UPb age. *Chemical Geology*, *511*, 1-10.

Wiedenbeck, M.A.P.C., Alle, P., Corfu, F., Griffin, W.L., Meier, M., Oberli, F.V., Quadt, A.V., Roddick, J.C. and Spiegel, W. (1995). Three natural zircon standards for U-Th-Pb, Lu-Hf, trace element and REE analyses. *Geostandards newsletter*, *19*(1), 1-23.

Wilde, S. A., Valley, J. W., Peck, W. H., & Graham, C. M. (2001). Evidence from detrital zircons for the existence of continental crust and oceans on the Earth 4.4 Gyr ago. *Nature*, *409*(6817), 175.

Wyche, S., Nelson, D. R., & Riganti, A. (2004). 4350–3130 Ma detrital zircons in the Southern Cross Granite-Greenstone Terrane, Western Australia: implications for the early evolution of the Yilgarn Craton. *Australian Journal of Earth Sciences*, *51*(1), 31-45.

FIGURES

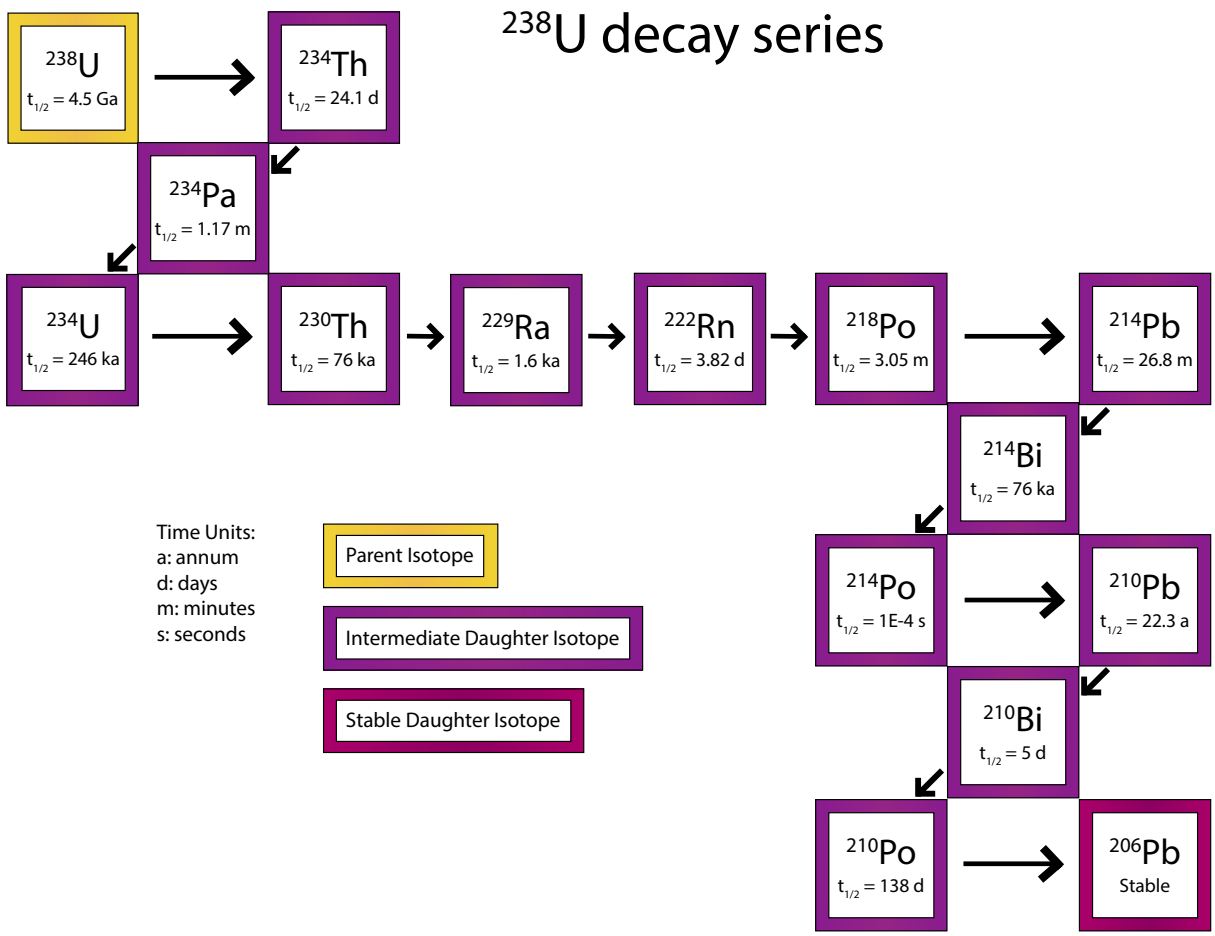

Figure 1: ^{238}U decay series. Half-lives are listed below each element. Notice that ^{230}Th and ^{234}U are the only elements within this decay chain with half-live longer than ~2 ka. Zircon does not isotopically fractionate U, so ^{234}U is not affected.

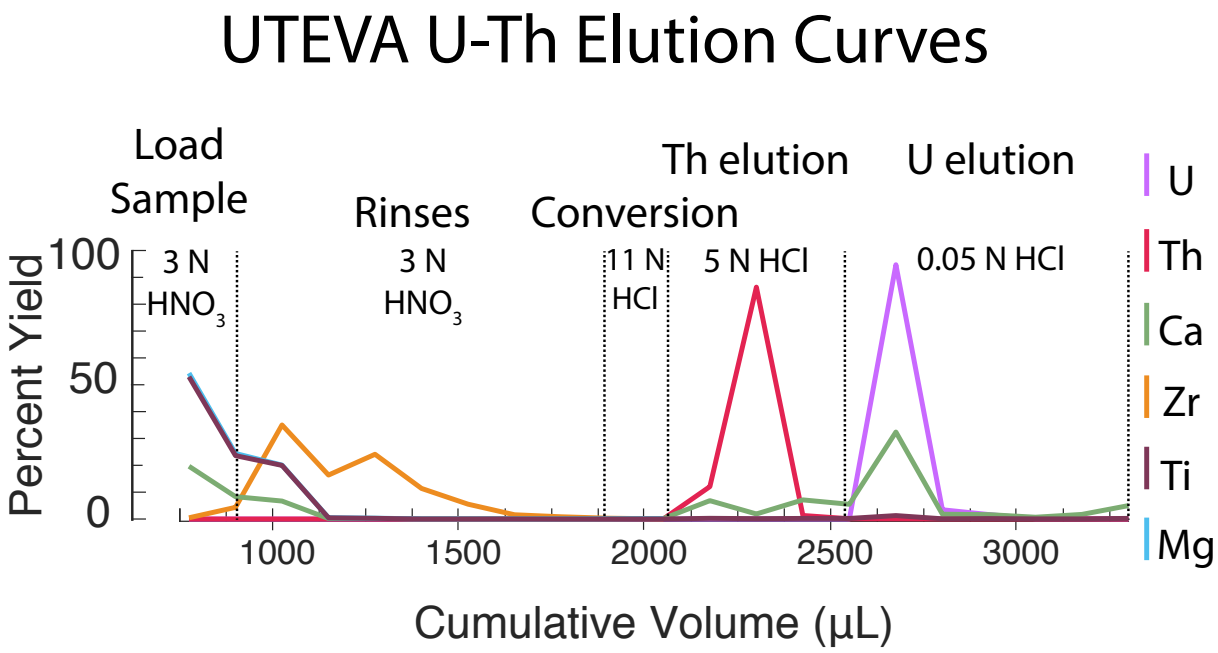

Figure 2: Column calibration curve for dissolved experimental H049 andesitic glasses on 50 µL UTEVA columns, miniaturizing the procedure of Tissot and Dauphas (2015). This procedure separates U and Th into separate aliquots. By separating U and Th from major elements in the zircons, such as Si and Zr, this procedure eliminates matrix effects or mass interference that could affect U and Th analyses.

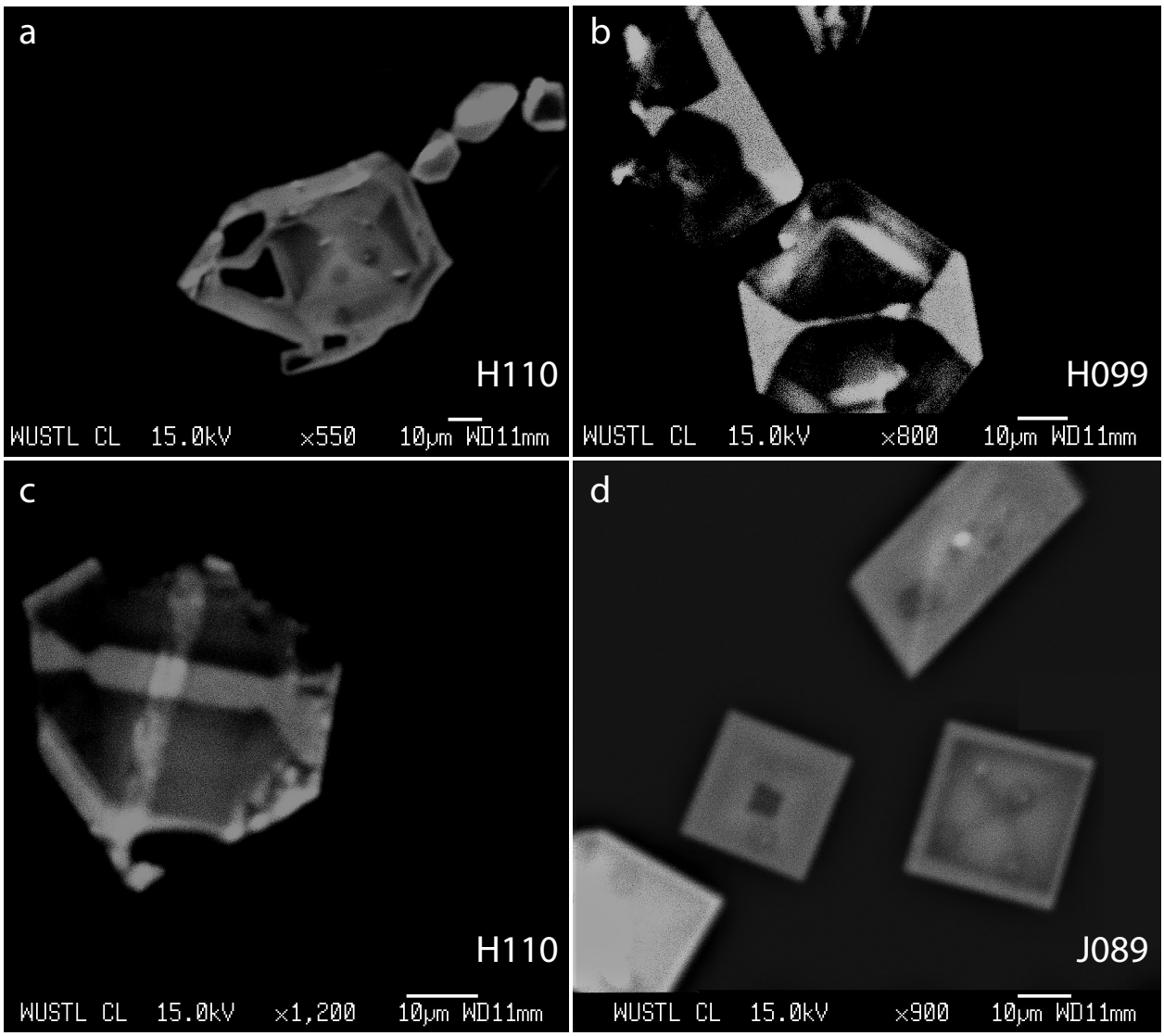

Figure 3: CL images of samples H110, H099, and J089 showing sector zoning in zircon crystals. Some images (a, c, d) have CL-light rims.

(a) Zircons in this CL image of H110 has a typical sector zoning pattern. The largest zircon is interpreted to have *c* axis parallel to the mount. Sector zoning occurs when a particular side of the crystal becomes more energetically favorable for atoms to join the crystal lattice. A glass shard with zircons in it was mounted onto an epoxy mount for EMPA analyses. The electron beam spot size was 3 μm.

(b) A zircon in the center of the H099 image also has typical sector zoning patterns since the crystal is placed with the c-axis parallel to the mount. In this crystal, dark zones are more prevalent than light zones. Zircon was mounted in a small shard of glass on an epoxy mount and analyzed after SIMS analysis.

(c) This H110 zircon was hand-picked onto an epoxy mount. We've interpreted that this zircon was placed on the mount with its c-axis perpendicular to the mount, which is why it exhibits an unusual zoning pattern.

(d) These J089 crystals appear square. A glass shard containing these crystals was mounted in an epoxy mount for EMPA analyses, so orientation was not controlled. Spot sizes were 3 μm. These crystals appear to have their c-axes perpendicular to the mount. They still show some zoning patterns, and CL-light rims.

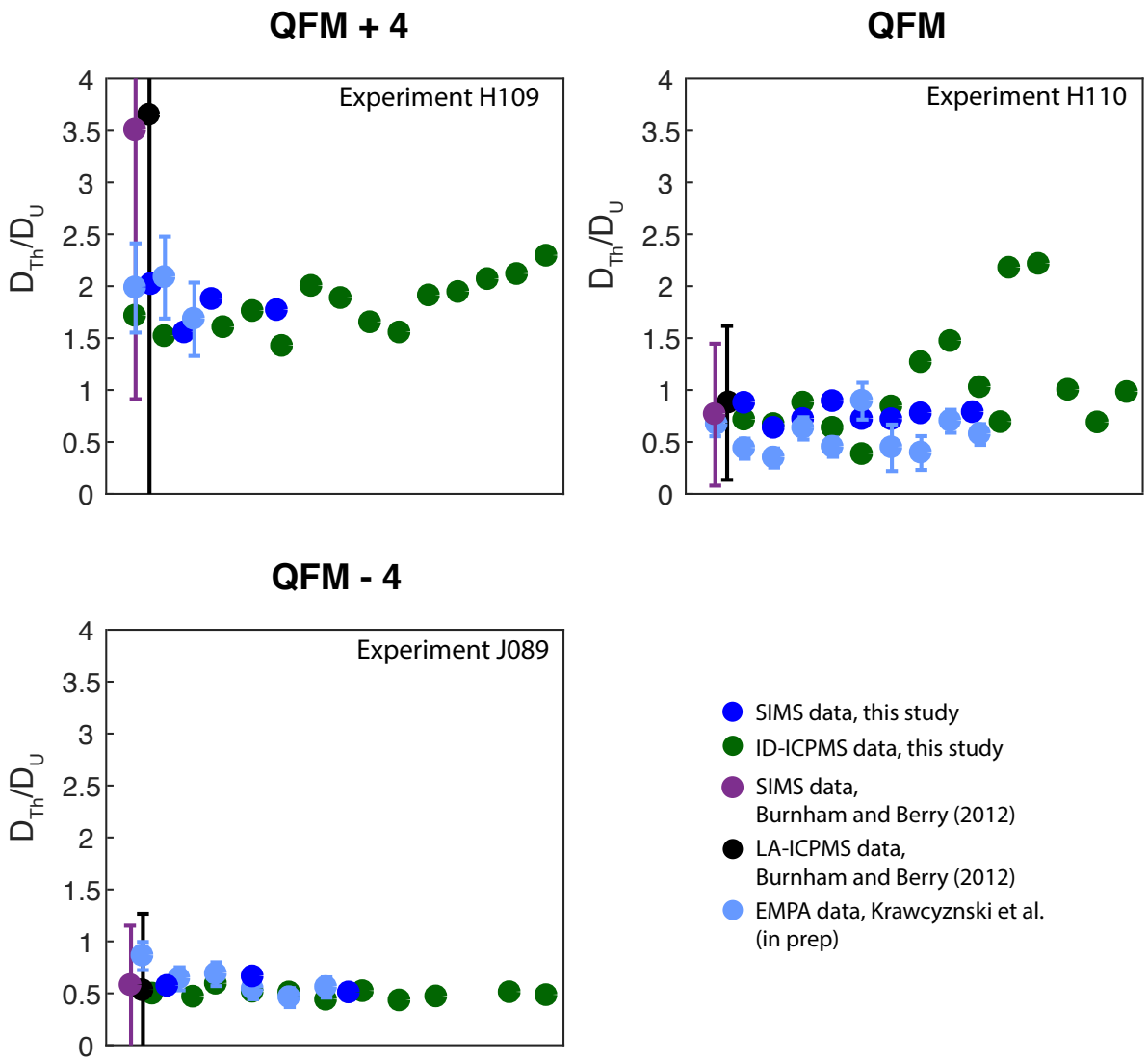

Figure 4: D_{Th}/D_U of zircon across a range of oxygen fugacities. Ratios were calculated by comparing the individual grain $^{232}Th/^{238}U$ ratio to the weighted mean of the ~5 glass shard analyses for each sample. Green points are ID-ICPMS data from this study. Blue points are SIMS data from this study. Purple and black filled circles are from Burnham and Berry (2012). Uncertainties are 2σ analytical for all data. Circles without error bars had uncertainties smaller than the data point. Variation between individual grains in ID-ICPMS data and SIMS data has been attributed to sampling across different sector zones. The uncertainties from Burnham and Berry (2012) encompass the entire range of f values from our study. These oxygen fugacity

conditions range from lower mantle to upper crustal f_{O2}. SIMS and EMPA data tend to bracket the whole-crystal ID-ICPMS data, since the spot analyses are able to sample the highest and lowest D_{Th}/D_U ratios in light and dark sectors. We attribute all the variability in these measurements to sector zoning, except the four outlier ID-ICPMS measurements in the QFM plot, as observed in the CL images in Fig. 3 and 6. These four data are likely the result of residual glass in our analyses. It is also possible that EMPA and SIMS measurements were not able to sample the extreme D_{Th}/D_U values of the dataset based on the number we sampled.

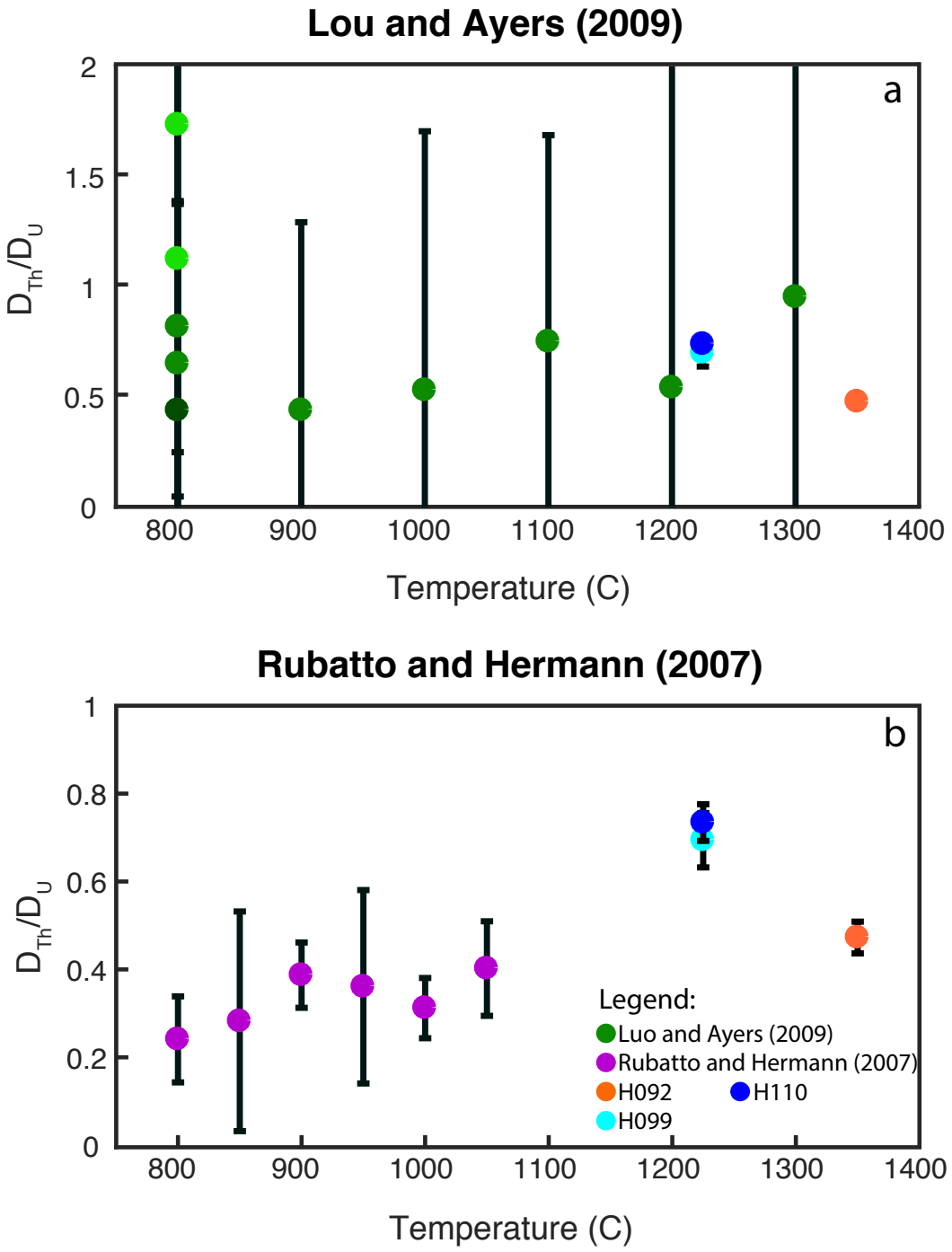

Figure 5: f values calculated from Rubatto and Hermann (2007) and Luo and Ayers (2009) across a temperature range. Error bars are 2σ. Rubatto and Hermann (2007) data are represented by purple points, and Luo and Ayers (2009) data are shown as green points. Weighted means

from the andesite experiment (H092) are represented by orange points. Weighted mean data from the basaltic andesite samples are represented by cool colored points. Samples J089 (QFM-4), H109 (QFM+4), and J096 (QFM-4) were excluded from this figure since these experiments were grown under different f_{O2} conditions than H099, H110, and H092 (all QFM).

(a) f values from Luo and Ayers vary at 800 C within uncertainty. These experiments were grown at 0.1 and 0.2 Gpa with different f_{O2} buffers (NNO, HM, IW). Pressure does not appear to affect D_{Th}/D_U ratios. Experiments grown with the HM buffer (light green) have the highest f values, while experiments grown with the NNO (green) and IW (dark green) buffers have much lower D_{Th}/D_U. Two experiments from the Luo and Ayers (2009) dataset are excluded from Fig. 5 because they greatly exceed the range of D_{Th}/D_U ratios.

(b) f values from Rubatto and Hermann (2007) increase with temperature implying that Th partitioning increases slightly relative to U. Basaltic andesites (H099 and H110) agree with the general pattern of increase with temperature. Andesitic experiment H092 decreases compared to the basaltic andesites implying that composition could also affect D_{Th}/D_U.

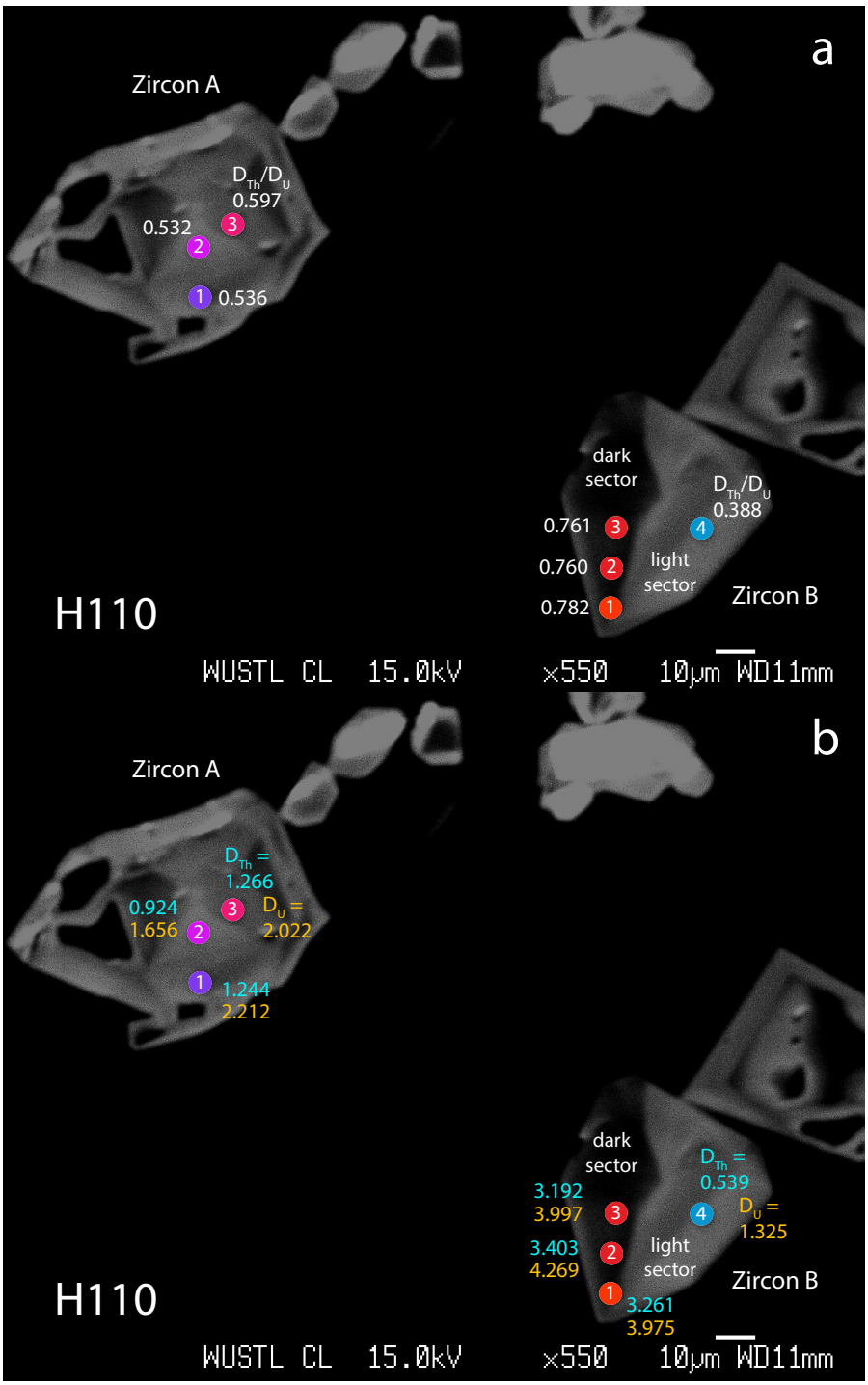

Figure 6: EMPA spot locations on two zircons in H110, a basaltic andesite experiment conducted at an f_{O2} at QFM buffer boundary.

(a) Warmer colors represent higher D_{Th}/D_U while cooler colors represent lower f values. D_{Th}/D_U does not vary based on the size of the grain or size of the sector within sample H110. Uncertainties range from 0.092 to 0.120, 2σ absolute.

(b) Individual D_{Th} and D_U from EMPA measurements from Krawczynski et al. (in prep) are shown. Blue values are D_{Th} and D_U is represented by yellow values. D_{Th} and D_U can vary more dramatically than D_{Th}/D_U within a single zircon. In zircon A, spots 1 and 2 appear to be located within the same CL-bright sector. The U and Th partition coefficients for these two spots decrease moving away from the crystal's center. In zircon B, three spots are located in a CL-dark sector. These spots have much higher partition coefficients than the spot in the bright sector. Uncertainties range from 0.074 to 0.438, 2σ absolute.

TABLES

Table 1: UTEVA cation exchange column chromatography procedure

Step:	**Acid:**	**Amount:**
Clean Resin	0.05 N HCl	500 µL total: 2x 250 µL
Condition	3 N HNO3	150 µL
Load Sample in 3 N HNO3	Sample + 3 N HNO3	250 µL
Bulk rinse	3 N HNO3	1000 µL total: 4x 250 µL
Conversion step	11 N HCl	150 µL
Elute Th	5 N HCl	500 µL total: 2x 250 µL
Elute U	0.05 N HCl	750 µL total: 3x 250 µL
After chemistry:		
Dry Down U and Th aliquots on a hotplate at ~130 C		

Table 2: Starting compositions for experiments from Krawczynski et al., (in prep).

Oxide (wt %)	Andesite (A)	Basaltic andesite (BA)
SiO_2	57.3	49.1
TiO_2	0.7	0.60
Al_2O_3	16.5	15.6
FeO	4.3	7.5
MnO	0	0.2
MgO	2.3	10.3
CaO	6.9	9.20
Na_2O	3.6	2.1
K_2O	1.5	0.4
P_2O_5	0	0.1
ZrO_2	7.0	5.0
M value	2.0	2.81

Table 3: Starting experimental parameters for ID-ICPMS analyzed samples synthesized by Krawczynski et al., (in prep).

Sample	Composition	Doped Th (ppm)	Doped U (ppm)	f_{O2}	Cooling rate (C/hr)	Start temperature (C)	End temperature (C)
H110	BA	1000	1000	QFM	10	1325 C	1225
H109	BA	1000	1000	QFM+4	10	1325 C	1225
J096	A	500	500	QFM-4	10	1400 C	1325
H099	BA	1000	1000	QFM	10	1325 C	1225
J089	BA	1000	1000	QFM-4	10	1325 C	1225
H092	A	500	500	QFM	2	1410 C	1350

Table 4: Summary of parameters for the KU 66-112 gravimetric solution.

U source metal	CRM 112a
Th source powder	CRM 66-7
U metal mass (g)[1]	0.6377188 ± 0.0000044
ThO_2 powder mass (g)[1]	1.4941937 ± 0.0000073
U metal purity[2]	0.999777 ± 0.00006
ThO_2 powder purity[2]	0.9999402 ± 0.0000062
$^{238}U/^{235}U$[3]	137.844 ± 0.024
$^{232}Th/^{238}U$	2.11932 ± 0.00011

[1] Corrected for mass of air displaced by ThO_2 powder and aluminum boat and U metal during weighing. Uncertainties reported are 2s and include all sources of random and systematic uncertainty.

[2] Certificate values (NBL, 2010, 2008)

[3] CRM 112a isotopic composition from Condon et al. (2010)

Table 5: Summary of parameters used to make KU 229-235 isotopic tracer. Weighted mean isotope ratios for U and Th isotopic compositions.

Tracer U IC: $^{238}U/^{235}U$[1]	0.005635 ± 0.000011
Tracer Th IC: $^{232}Th/^{229}Th$[2]	0.000344 ± 0.000004
Tracer $^{235}U/^{229}Th$	1.7893 ± 0.0048

[1] KU4A-1 gravimetric solution of ^{235}U made from SRM 970

[2] Cottle Th solution

Table 6: ID-ICPMS data for zircon megacryst 91500.

Source	91500 Th/U ratio	Analytical uncertainty
grain fragment 1	0.3680	0.0588[1]
grain fragment 2	0.3749	0.0213[1]
grain fragment 3	0.3540	0.0211[1]
Weighted mean, this study	0.3549	0.0121[2]
Wiedenbeck et al. (1995)	0.3444	0.0009[2]

[1] 2σ analytical uncertainty

[2] weighted mean uncertainty (2σ), MSWD

Table 7: SIMS, EMPA, ID-ICPMS data for six experiments analyzed in this study.

Sample	f_{O2}	Melt Composition	Temperature (C)	Dark D_U	Dark D_{Th}	Light D_U	Light D_{Th}	Dark D_{Th}/D_U	Light D_{Th}/D_U	Crystal D_{Th}/D_U[3]	Uncertainty (2σ)[4]	Crystal D_{Th}/D_U[5]	Uncertainty (2σ)[4]
J089	QFM-4	BA[1]	1225	3.82	2.04	2.06	0.78	0.53	0.38	0.5761	0.0776	0.5935	0.0023
H099	QFM	BA	1225	3.13	2.36	1.93	1.13	0.75	0.59	0.6986	0.0618	-	-
H110	QFM	BA	1225	3.27	2.47	1.13	0.49	0.76	0.43	0.7388	0.0417	0.7423	0.0013
H109	QFM+4	BA	1225	1.10	2.30	0.86	1.46	2.08	1.68	1.7590	0.0163	1.8214	0.0049
J096	QFM-4	A[2]	1325	-	-	-	2.59	1.18	0.45	0.4393	0.0110	-	-
H092	QFM	A	1350	-	-	-	1.56	0.70	0.45	0.4773	0.0361	-	-

[1]Basaltic andesite melt composition (Table 2).
[2]Andesitic melt composition (Table 2).
[3]Weighted mean D_{Th}/D_U from ID-ICPMS analyses
[4]2σ weighted mean uncertainty
[5]Weighted mean D_{Th}/D_U from SIMS analyses

APPENDICIES

Appendix A: ID-ICPMS Metadata

Laboratory and Sample Preparation	
Laboratory name	KU Geology Isotope Geochemistry Laboratories
Sample type/mineral	Zircon, glass
Sample Preparation	Crushing with mortar and pestle, hand picking, leaching with cold HF, dissolution, UTEVA column chemistry
ICPMS Instrument	
Make, Model, and Type	Thermo Element2 magnetic sector field ICPMS
Sample introduction	1 N HNO_3 + 0.005 N HF solution aerosol, with ESI PC3 spray chamber and ESI SC-E2 autosampler
Sample uptake	~200 μL/min
Sample gas flow	1.045 to 1.078 L/min
RF power	1018 to 1071 W
Auxiliary gas flow	0.96 to 0.96 L/min
Detection system	MasCom secondary electron multiplier
Masses measured	^{229}Th, ^{232}Th, ^{235}U, ^{238}U
Integration time per peak (ms)	
Total integration time per reading (s)	
Total method time (s)	
IC dead time (ns)	4
UO+/U+ ratio (%)	~5
Sensitivity	2E6 to 4E6 cps for 1 ppb ^{238}U solution, 2.5 ‰
Data Processing	
Calibration strategy	CRM 112a (in KU 66-112 solution) $^{238}U/^{235}U$ ratio used for mass fractionation corrections of both U and Th
Reference Material Information	CRM 112a (Condon et al., 2010)
Uncertainty level and propagation	DTh/DU ratios propagated to 2σ
Reproducibility	

Appendix B: ID-ICPMS data

Table B1: Experimentally determined $^{232}Th/^{238}U$ and f values measured by ID-ICPMS

Sample	$^{232}Th/^{238}U$	1σ	D_{Th}/D_U	2σ	Sample	$^{232}Th/^{238}U$	1σ	D_{Th}/D_U	2σ
H109-1	2.655	0.015	1.710	0.051	H110-1	0.935	0.014	0.686	0.036
H109-2	2.352	0.014	1.515	0.047	H110-2	0.968	0.014	0.710	0.037
H109-4	2.485	0.013	1.601	0.047	H110-3	0.909	0.012	0.667	0.032
H109-5	2.726	0.014	1.756	0.051	H110-4	1.191	0.015	0.874	0.041
H109-6	2.205	0.013	1.420	0.043	H110-5	0.861	0.016	0.632	0.037
H109-7	3.102	0.013	1.998	0.054	H110-6	0.516	0.014	0.379	0.029
H109-8	2.921	0.013	1.881	0.052	H110-7	1.140	0.015	0.837	0.040
H109-9	2.558	0.015	1.648	0.050	H110-8	1.722	0.016	1.264	0.051
H109-10	2.406	0.014	1.550	0.047	H110-9	1.999	0.014	1.467	0.053
H109-11	2.960	0.014	1.906	0.053	H110-10	1.394	0.013	1.023	0.042
H109-12	3.011	0.014	1.939	0.054	H110-11	2.960	0.015	2.172	0.070
H109-13	3.204	0.013	2.064	0.055	H110-12	3.011	0.018	2.210	0.075
H109-14	3.280	0.013	2.112	0.056	H110-13	1.360	0.015	0.998	0.044
H109-15	3.553	0.013	2.289	0.059	H110-14	0.931	0.015	0.683	0.037
					H110-15	1.330	0.016	0.976	0.045
H109-G1	1.416	0.014			H110-G1	1.416	0.015		
H109-G2	1.525	0.014			H110-G2	1.027	0.015		
H109-G3	1.549	0.014			H110-G3	1.591	0.015		
H109-G4	1.574	0.014			H110-G4	1.415	0.015		
H109-G5	1.700	0.014							

Table B1: Experimentally determined $^{232}Th/^{238}U$ and f values measured by ID-ICPMS

Sample	$^{232}Th/^{238}U$	1σ	D_{Th}/D_U	2σ	Sample	$^{232}Th/^{238}U$	1σ	D_{Th}/D_U	2σ
H099-1	1.189	0.028	0.796	0.082	J089-1	0.804	0.021	0.477	0.031
H099-2	0.981	0.029	0.657	0.076	J089-2	0.830	0.019	0.493	0.029
H099-3	1.216	0.029	0.814	0.084	J089-3	0.780	0.019	0.463	0.029
H099-4	1.050	0.026	0.703	0.074	J089-4	0.991	0.019	0.588	0.031
H099-5	0.990	0.025	0.663	0.071	J089-5	0.860	0.020	0.511	0.030
H099-6	1.106	0.031	0.741	0.083	J089-6	0.849	0.019	0.504	0.030
H099-7	1.219	0.034	0.816	0.091	J089-7	0.730	0.019	0.434	0.029
H099-8	0.975	0.033	0.653	0.082	J089-8	0.869	0.019	0.516	0.030
H099-9	1.009	0.042	0.675	0.094	J089-9	0.720	0.019	0.427	0.028
H099-10	1.051	0.029	0.704	0.078	J089-10	0.784	0.019	0.465	0.029
H099-11	0.982	0.029	0.658	0.075	J089-12	0.852	0.019	0.506	0.030
H099-12	0.923	0.026	0.618	0.069	J089-13	0.805	0.019	0.478	0.029
					J089-G1	1.709			
H099-G1	0.982	0.025			J089-G2	1.794			
H099-G3	1.493	0.037			J089-G3	1.757			
H099-G4	1.152	0.033			J089-G4	1.480			

Table B1: Experimentally determined $^{232}Th/^{238}U$ and f values measured by ID-ICPMS

Sample	$^{232}Th/^{238}U$	1σ	D_{Th}/D_U	2σ	Sample	$^{232}Th/^{238}U$	1σ	D_{Th}/D_U	2σ
J096-1	3.043	0.013	0.391	0.005	H092-1	0.548	0.018	0.477	0.058
J096-2	4.345	0.013	0.558	0.006	H092-2	0.476	0.018	0.414	0.055
J096-3	3.205	0.013	0.411	0.005	H092-4	0.265	0.018	0.231	0.046
J096-4	3.345	0.013	0.429	0.005	H092-5	0.498	0.018	0.434	0.057
J096-5	4.696	0.013	0.603	0.006	H092-6	0.723	0.019	0.629	0.069
J096-6	3.737	0.013	0.480	0.005	H092-7	7.137	0.017	6.215	0.391
J096-7	3.304	0.013	0.424	0.005	H092-8	1.471	0.018	1.281	0.106
J096-8	2.954	0.013	0.379	0.005	H092-9	0.849	0.019	0.739	0.076
J096-9	3.310	0.013	0.425	0.005	H092-10	0.513	0.018	0.447	0.058
J096-10	5.116	0.013	0.657	0.006	H092-11	0.903	0.019	0.786	0.078
J096-11	3.306	0.013	0.424	0.005	H092-12	1.919	0.018	1.671	0.128
J096-12	3.302	0.013	0.424	0.005					
J096-13	3.498	0.013	0.449	0.005					
J096-14	3.307	0.012	0.425	0.005					
J096-15	3.091	0.013	0.397	0.005					
J096-G1	8.793	0.015			H092-G1	1.057	0.025		
J096-G2	7.206	0.015			H092-G4	1.240	0.033		
J096-G4	7.515	0.017							
J096-G5	7.643	0.015							

Appendix C: SIMS data

Table C1: Experimentally determined $^{232}Th/^{238}U$ and f values measured by SIMS

Sample	$^{238}U^{16}O/^{232}Th^{16}O$	% std error	$^{232}Th/^{238}U$	1σ	f	2σ
H109 zrc1, spot 1	0.2836	0.0738	3.7548	0.0028	2.016	0.009
H109 zrc1, spot 2	0.3687	0.2014	2.8885	0.0058	1.551	0.011
H109 zrc2, spot 1	0.3054	0.1161	3.4870	0.0040	1.872	0.010
H109 zrc2, spot 2	0.3239	0.1192	3.2879	0.0039	1.765	0.009
H109 glass, spot 1	0.4971	0.1759	1.8531	0.0033		
H109 glass, spot 2	0.5005	0.1282	1.8404	0.0024		
H109 glass, spot 3	0.5020	0.1860	1.8350	0.0034		
H109 glass, spot 4	0.5046	0.1570	1.8255	0.0029		
H109 glass, spot 5	0.4868	0.1349	1.8921	0.0026		
H109 glass, spot 6	0.4868	0.1337	1.8920	0.0025		
H109 glass, spot 7	0.4901	0.1595	1.8794	0.0030		
H109 glass, spot 8	0.4887	0.1176	1.8849	0.0022		

Table C1: Experimentally determined $^{232}Th/^{238}U$ and f values measured by SIMS

Sample	$^{238}U^{16}O/^{232}Th^{16}O$	% std error	$^{232}Th/^{238}U$	1 σ	f	1 σ
H110 zrc1, spot 2	0.7470	0.1111	1.4328	0.0016	0.7819	0.0041
H110 zrc2, spot 1	0.6693	0.1109	1.5989	0.0018	0.8726	0.0046
H110 zrc3, spot 1	0.9254	0.1063	1.1565	0.0012	0.6311	0.0033
H110 zrc3, spot 2	0.8160	0.1017	1.3116	0.0013	0.7157	0.0036
H110 zrc4, spot 1	0.6540	0.1341	1.6284	0.0022	0.8886	0.0051
H110 zrc4, spot 2	0.8121	0.1397	1.3114	0.0018	0.7156	0.0042
H110 zrc4, spot 3	0.8140	0.0695	1.3084	0.0009	0.7140	0.0032
H110 glass, spot 1	0.7540	0.0610	1.4125	0.0009		
H110 glass, spot 2	0.5201	0.1815	1.7815	0.0032		
H110 glass, spot 3	0.4996	0.1475	1.8543	0.0027		
H110 glass, spot 4	0.5000	0.1320	1.8530	0.0024		
H110 glass, spot 5	0.5125	0.1480	1.7975	0.0027		
H110 glass, spot 6	0.4982	0.1624	1.8492	0.0030		

Table C1: Experimentally determined $^{232}Th/^{238}U$ and f values measured by SIMS

Sample	$^{238}U^{16}O/^{232}Th^{16}O$	% std error	$^{232}Th/^{238}U$	1 σ	f	1 σ
J089 zrc1, spot 1	1.1350	0.1017	0.9246	0.0009	0.5037	0.0028
J089 zrc2, spot 1	1.0085	0.8511	1.0406	0.0089	0.5668	0.0116
J089 zrc2, spot 2	0.5051	0.1365	2.0778	0.0028	1.1318	0.0070
J089 zrc2, spot 3	0.8687	0.4460	1.2080	0.0054	0.6580	0.0081
J089 glass, spot 1	0.5027	0.1574	1.8427	0.0029		
J089 glass, spot 2	0.5038	0.2204	1.8387	0.0041		
J089 glass, spot 3	0.5055	0.1643	1.8322	0.0030		
J089 glass, spot 4	0.5057	0.1818	1.8318	0.0033		
J089 glass, spot 5	0.5045	0.1622	1.8302	0.0030		
J089 glass, spot 6	0.5020	0.1510	1.8394	0.0028		

Table C1: Experimentally determined $^{232}Th/^{238}U$ and f values measured by SIMS

Sample	$^{238}U^{16}O/^{232}Th^{16}O$	% std error	$^{232}Th/^{238}U$	1 σ
H092 glass, spot 1	0.6295	0.1894	1.4642	0.0028
H092 glass, spot 2	0.6885	0.2151	1.3387	0.0029
H092 glass, spot 3	0.6928	0.1817	1.3305	0.0024
H092 glass, spot 4	0.7171	0.1572	1.2853	0.0020
H092 glass, spot 5	0.7535	1.3087	1.2232	0.0160
H092 glass, spot 6	0.7140	0.1957	1.2909	0.0025
J096 glass, spot 1	0.1035	0.2194	8.9707	0.0197
J096 glass, spot 2	0.1095	0.2478	8.4849	0.0210
J096 glass, spot 3	0.1040	0.2118	8.9332	0.0189
J096 glass, spot 4	0.1025	0.3810	9.0363	0.0344
J096 glass, spot 5	0.1036	0.2838	8.9382	0.0254
J096 glass, spot 6	0.1029	0.2434	8.9983	0.0219
H099 glass, spot 1	0.5285	0.1658	1.7513	0.0029
H099 glass, spot 2	0.5279	0.1791	1.7531	0.0031
H099 glass, spot 3	0.5254	0.1543	1.7615	0.0027
H099 glass, spot 4	0.5328	0.2067	1.7370	0.0036
H099 glass, spot 5	0.5338	0.1698	1.7338	0.0029
H099 glass, spot 6	0.5489	0.1524	1.6862	0.0026
H099 glass, spot 7	0.5468	0.1260	1.6926	0.0021
H099 glass, spot 8	0.5518	0.1829	1.6774	0.0031